Exploring the Dust Content of Galactic Winds with *Herschel* II. Nearby Dwarf Galaxies[1]

Alexander McCormick[1], Sylvain Veilleux[1,2], Marcio Melendez[1], Crystal L. Martin[3], Joss Bland-Hawthorn[4], Gerald Cecil[5], Fabian Heitsch[5], Thomas Müller[6], David S. N. Rupke[7], Jordan Zastrow[8], Chad Engelbracht[9]

ABSTRACT

We present results from new, very deep *Herschel Space Observatory* data of six nearby dwarf galaxies with known galactic-scale winds. The improved resolution and light-collecting area of *Herschel* over previous infrared telescopes have allowed us to observe circumgalactic cold dust features on scales of ∼1.2-2.6 kpc, often well beyond the stellar component. Comparisons of these features with ancillary Hα, 8.0, and 24 μm data show an imperfect spatial correlation with the ionized gas and warm dust wind components. By spatially decomposing the cold dust emission into circumgalactic and stellar disk regions, we find that ∼10-30% of the total dust mass in these known wind galaxies resides outside their stellar disks, and ∼70% in the case of NGC 1569. Our data also hint at metallicity depletion via cold dust ejection as well as possible correlations of circumgalactic cold dust mass fraction and dust temperature with star formation rate surface density. However, these tantalizing implications are not formally statistically significant.

Subject headings: galaxies: intergalactic medium — galaxies: star formation — galaxies: structure — Infrared: galaxies — ISM: jets and outflows

---

[1]Department of Astronomy, University of Maryland, College Park, MD 20742, USA; E-mail: alexm@astro.umd.edu, veilleux@astro.umd.edu, marcio@astro.umd.edu

[2]Joint Space-Science Institute, University of Maryland, College Park, MD 20742, USA

[3]Department of Physics, University of California, Santa Barbara, CA 93106

[4]Department of Physics, University of Sydney, Sydney, NSW 2006, Australia

[5]Department of Physics, University of North Carolina, Chapel Hill, NC 27599

[6]Max-Planck-Institute for Extraterrestrial Physics (MPE), Giessenbachstrasse 1, 85748 Garching

[7]Department of Physics, Rhodes College, Memphis, TN 38112

[8]Department of Astronomy, University of Michigan, Ann Arbor, MI 48109

[9]Department of Astronomy, University of Arizona, Tucson, AZ 85721 (deceased)

1. INTRODUCTION

Galactic winds are a fundamental mechanism of galaxy evolution (see Veilleux et al. 2005 for a review). Simulations have shown that the outflows of material in winds can inhibit the growth of a central supermassive black hole and curb the galactic star formation rate (SFR) by removing its fuel (e.g. Di Matteo et al. 2005; Narayanan et al. 2008; Hopkins & Elvis 2010). Winds have also been invoked to explain a host of galaxy observations, including the mass-metallicity relation (Tremonti et al. 2004), the relation between central black hole mass and bulge velocity dispersion (Ferrarese & Merritt 2000; Gebhardt et al. 2000), and metal enrichment of the intracluster medium and intergalactic medium (Renzini 1997; Buote 2000). Furthermore, mounting evidence for galactic winds at $z > 1$ (e.g. Lowenthal et al. 1997; Pettini et al. 2001; Smail et al. 2003; Weiner et al. 2009) points to their importance in understanding the past history of the universe. Therefore, detailed observations of galactic winds are critical to fleshing out the narrative of galaxy evolution. Although negative feedback may assert even greater influence at high redshift, where strong starbursts and active galactic nuclei are more commonplace, nearby sources provide the best opportunities for detailed observations of the resultant winds. Investigating the winds of dwarf galaxies is particularly important due to the apparent metal depletion and lower star formation yield at the low end of the galactic mass distribution (Tremonti et al. 2004).

Prior to 2005, much of the observational data emphasized the entrained gas in winds from the neutral gas (Heckman et al. 2000; Rupke et al. 2002, 2005a,b,c; Schwartz & Martin 2004; Martin 2005) to ionized gas (Heckman et al. 1990; Lehnert & Heckman 1995) to the highly ionized X-ray emitting plasma (Read et al. 1997; Pietsch et al. 2000; McDowell et al. 2003; Ehle et al. 2004; Huo et al. 2004; Strickland et al. 2004a,b). Recent observations have shown that these outflows also entrain dust (Heckman et al. 2000; Tacconi-Garman et al. 2005; Engelbracht et al. 2006; Roussel et al. 2010; McCormick et al. 2013; Meléndez et al. 2015) and molecular gas (Veilleux et al. 2009; Fischer et al. 2010; Feruglio et al. 2010; Irwin et al. 2011; Sturm et al. 2011; Alatalo et al. 2011; Aalto et al. 2012). Dust grains found in the interstellar medium (ISM) were formed in the atmospheres of evolved stars or during the outbursts of novae and supernovae, but can also be destroyed and reconstituted in the ISM. Interstellar dust plays a crucial role in galaxy evolution and star formation, since it absorbs and scatters stellar light, it can act as the catalyst to form molecules through reactions not possible in the gas phase, it can either enrich the interstellar gas with heavy elements via destruction and evaporation of grains or deplete the gas via condensation on

[1] *Herschel* is an ESA space observatory with science instruments provided by European-led Principal Investigator consortia and with important participation from NASA.

grains, and electrons liberated from dust grains via the photoelectric effect can heat the ISM gas. Therefore, investigating the distribution, mass, and energy of the dust in wind galaxies provides critical information for understanding galaxy evolution. Observations of dusty winds may even catch galaxies in the act of expelling their star formation fuel, eventually halting that process (Roussel et al. 2010; Sturm et al. 2011; Bolatto et al. 2013; Veilleux et al. 2013; Cicone et al. 2014).

In this second paper of a series (Meléndez et al. 2015, hereafter Paper I), we investigate six nearby dwarf galaxies known to host galactic winds. For these sources, the resolution and sensitivity of previous far-infrared (FIR) data (e.g. *Spitzer* MIPS) are insufficient to test the properties of cool, shielded, wind-driven dust filaments or other features. The improved capabilities of the *Herschel Space Observatory* (Pilbratt et al. 2010) have allowed us to interpret the properties of cool circumgalactic dust in the winds of these nearby dwarf galaxies via new, very deep *Herschel* observations.

In § 2, we describe the selection criteria for our sample of nearby dwarf galaxies and provide tables summarizing their basic properties and the data we collected with *Herschel*. In § 3 and 4, we describe the data reduction process with example images and our analysis respectively. We present our results in § 5, including maps of each galaxy in *Herschel's* 70, 160, 250, 350, and 500 μm channels, and comparisons of circumgalactic dust properties with star formation and galactic stellar mass. Our results are summarized in § 6. Appendix A contains discussion of each individual galaxy and its features.

2. SAMPLE

We chose our sample of six nearby dwarf galaxies primarily due to previous evidence of galactic winds at other wavelengths. Table 1 lists the galaxies, some of their properties, and selected references to evidence of galactic winds for each source. From previous multi-wavelength observations, each of the galaxies hosts active star formation (H II regions), and one (He 2-10) contains both H II regions and an AGN. Due to their star formation rate (SFR) densities and the inferred ages of recent or ongoing star formation episodes, the galaxies in our sample are often characterized as starbursts. The membership of NGC 3077 in the M81 group complicates the interpretation of circumgalactic material, so we often represent it with a different symbol on plots and treat it separately in the discussion of results. Due to the presence of AGN activity in He 2-10 (Reines et al. 2011), we represent it with an open circle on plots to differentiate it from galaxies hosting just star formation.

We acquired very deep (> 6 hrs.) *Herschel Space Observatory* PACS (Poglitsch et al.

2010) images in the 70 and 160 μm infrared (IR) channels for each of the six dwarfs in our sample as part of a two stage observational program to investigate nearby star-forming galaxies. Each of the 70 and 160 μm PACS observations consisted of seven scan 'legs.' Orienting each of the seven scan legs at a different angle virtually eliminates systematic noise from low-level striping and reaches approximately Poisson noise limits. We also acquired SPIRE (Griffin et al. 2010) data at 250, 350, and 500 μm for the one galaxy in our sample which had not already been observed (NGC 1800) and downloaded archived SPIRE data for the other five galaxies. The SPIRE observations were performed in the LargeScanMap mode using orthogonal scan directions and multiple iterations for four out of the six galaxies (single iterations: He 2-10 and NGC 1569). The *Herschel* data are summarized in Table 2.

In additional to the new *Herschel* data we acquired, we also brought together ancillary data for each galaxy in four additional bands: Hα, 4.5, 8.0, and 24 μm. A few different observers collected the Hα data, and we downloaded the IR data from the *Spitzer* archive for IRAC (4.5 and 8.0 μm) and MIPS (24 μm). The ancillary data are summarized in Table 3.

3. DATA REDUCTION

After the *Herschel* observations were performed between January 2012 and March 2013, we obtained the new PACS and SPIRE data from the *Herschel* Science Archive (HSA). We downloaded the archival *Spitzer* Infrared Array Camera (IRAC) and Multiband Imaging Photometer (MIPS) data from the NASA/IPAC Infrared Science Archive. Before performing any reduction, we briefly examined the new *Herschel* data with version 10.3.0 of the Herschel Interactive Processing Environment (HIPE; Ott 2010), and we also inspected the Hα data and pipeline-processed *Spitzer* data (PBCDs) using SAOImage DS9.

3.1. *Herschel* Data Reduction

We reprocessed our *Herschel* data with HIPE up to Level-1 employing the PACS photometer pipeline (Wieprecht et al. 2009) and then passed these data on to the *Scanamorphos* v21 software(Roussel 2013). Since our deep *Herschel* observations aimed to detect very faint emission from cold dust in circumgalactic wind regions, we employed *Scanamorphos*, which was built specifically to handle scan mode observations like ours, the preferred acquisition mode for nearby galaxies. *Scanamorphos* exploits the redundancy of the observations in order to subtract low frequency noise due to thermal and non-thermal components. It also masks high frequency artifacts like cosmic ray hits before projecting the data onto a map. The final pixel sizes are 1.4, 2.85, 4.5, 6.25, and 9.0 arcseconds for the 70, 160, 250, 350, and 500 μm maps respectively. The *Herschel* maps are shown in Figures 1a - 1f along with the ancillary Hα, 4.5, 8.0, and 24 μm data.

3.2. *Spitzer* Data Reduction

Our reduction of the *Spitzer* IRAC data followed the same procedures as those described in McCormick et al. (2013), summarized here. Starting from the basic calibrated data, we corrected any electronic and optical banding in the 8.0 μm channel. Several of our sample galaxies' bright nuclei generate broad point spread functions (PSFs) in both the 4.5 and 8.0 μm channels, which overlap with circumgalactic regions, so we subtracted the wings of any broad PSFs using the APEX and APEX QA modules of the *Spitzer Science Center*-provided MOPEX software (Makovoz & Khan 2005). Where necessary, we also performed a background subtraction to better distinguish background flux from circumgalactic features. Once the basic calibrated data were processed, we created maps of both channels using MOPEX. For NGC 1569, NGC 1705, and NGC 5253, we used the previously-reduced data presented in McCormick et al. (2013).

4. DATA ANALYSIS

4.1. Disk-Circumgalactic Decomposition

Differentiating between a galaxy and its circumgalactic or extraplanar or halo region necessitates defining an edge or border between the two when analyzing a image projected on the sky. In McCormick et al. (2013), we defined this edge by applying two different methods to the predominantly stellar emission of the IRAC 4.5 μm channel, which generated very similar regions when both methods were workable. The first method employed a fitted scale height in the case of sufficiently edge-on galaxies. The second method used the standard deviation of the 4.5 μm background noise and a 20σ contour to delineate the galaxy from the circumgalactic regions. We applied the second method to each of the three galaxies in this study's sample, which do not overlap with the sample found in McCormick et al. (2013); He 2-10, NGC 1800, and NGC 3077. We used the previously-generated regions for NGC 1569 (scale height), NGC 1705 (20-σ), and NGC 5253 (20-σ). For the sake of consistency, we will call all of these 'disk' regions, although most of the galaxies don't exhibit a classical disk morphology. The flux regions are shown in Figures 4a - 4f. The circumgalactic flux region for NGC 1569 is necessarily conservative, because of the proximity of Galactic cirrus, which are noticeably impinging on the circumgalactic region in the SPIRE maps (see Figure 1b).

4.2. Removal of the Disk PSFs with a CLEAN Algorithm

In both the PACS and SPIRE instruments, the PSFs are broad enough that the wings from bright disk region sources bleed out and contribute significant excess flux to the circumgalactic regions where we're looking for just the faint circumgalactic dust emission. To subtract this excess, we employed a modified version of the CLEAN algorithm[2] (Högbom 1974). Our CLEAN algorithm finds the peak pixel within an area similar to the disk region, subtracts the appropriate PSF scaled by a pre-defined gain as a fraction of the peak pixel value, and repeats these two steps until the peak pixel value meets or drops below a pre-defined minimum threshold value. Once the minimum threshold value is reached, the algorithm outputs component and residual images. Since the galaxies in our sample contain broad, bright areas within their disk regions, we chose PSFs from Vesta (Obs. IDs 1342195624, 1342195625) and Uranus (Obs. ID 1342197342), which are extended sources rather than strict point sources. We selected *Herschel* observations of Vesta and Uranus with the same scan speed as our observations, which is important for matching the shape of the PSFs. We processed the PSFs through the same combination of HIPE and *Scanamorphos* as described in § 3.1. Next, we rotated the PSFs to match the galaxy observations, centered the PSFs on their central pixels, and scaled the PSFs by normalizing their central peak pixels to a value of 1 for gain multiplication. Finally, we applied our CLEAN algorithm to each of the PACS and SPIRE images iteratively lowering the threshold value to determine a circumgalactic flux value convergence. Figure 3 illustrates the before and after results of applying our CLEAN algorithm to the maps of NGC 1569. We find the excess flux contribution from the disk to the circumgalactic region across all bands has a mean and median of $\sim$ 40-50% with a standard deviation of $\sim$ 15% and no obvious trend with wavelength. Residual maps after application of our CLEAN algorithm are shown in Figures 4a - 4f.

4.3. *Herschel* Flux Measurements

We made two flux measurements - global and circumgalactic - in each of the five *Herschel* bands. The global flux measurement came from a circular or elliptical aperture containing the most extended circumgalactic cold dust features exhibited by each galaxy. We measured

[2] Adapted from http://www.mrao.cam.ac.uk/~bn204/alma/python-clean.html.

the global flux in the original maps. Note that the most extended features did not always appear in the same *Hershel* band. The circumgalactic flux was measured from the CLEAN residual image by subtracting the residual flux within the disk region from the flux in the global region. The disk flux was then calculated by subtracting this circumgalactic flux from the global flux measured in the original map. Using this method, the excess flux that bled out of the disk region into the circumgalactic region is added back into the disk flux total. We also took sample flux measurements in clean, uncontaminated sky regions outside the global flux regions to confirm whether *Scanamorphos* had properly removed the background in the *Herschel* maps. The background regions in the PACS maps contained flux values close enough to zero as to be indistinguishable from noise. However, the backgrounds of the SPIRE maps still contained enough flux from either background sources or residual noise to require a background correction. We measured the flux in background regions identical in size and shape to the global region tiled around the global region perimeter. We then averaged these background fluxes and subtracted the average to get the final SPIRE global flux measurement. The SPIRE background contribution fell somewhere in the 2-14% range (mean $\sim$ 8%) with NGC 1569 as an outlier at about 20% likely due to a contribution from the nearby Galactic cirrus. We adopted a conservative flux calibration uncertainty of 10%, which consists of the systematic (4-5%), statistical (1-2%), and PSF/beam size (4%) uncertainties. Derived aperture corrections of order $\sim$ 1-2% (see Paper I) are easily dwarfed by this calibration uncertainty. The global, disk, and circumgalactic flux values are listed in Table 4.

4.4. Spectral Energy Distribution (SED) Fitting

In order to characterize the cold dust of each galaxy in our sample, we fit a modified blackbody (MBB) following the one found in Section 3.1 of Smith et al. (2012). We fit the sets of 70, 160, 250, 350, and 500 μm global and disk flux values to:

$$S_\nu = \frac{M_d \, \kappa_\nu \, B_\nu(T_d)}{d^2} \tag{1}$$

where M_d and T_d are the dust mass and temperature respectively, d is the distance to the galaxy listed in Table 1, B_ν is the Planck function, and κ_ν is the dust absorption coefficient which has a power law dependence with dust emissivity index β where $\kappa_\nu = \kappa_0(\nu/\nu_0)^\beta$. κ_0 is the dust opacity at $\nu_0 = 350$ μm: 0.192 m^2 kg^{-1} (Draine 2003). We fit the parameters M_d, T_d, and β to each set of global and disk fluxes determining values for M_{global}, T_{global}, M_{disk}, T_{disk}. The fits also included the 10% flux calibration uncertainties. Fitting all three parameters often produced unphysical β values, so instead we fit just M_d and T_d and adopted a fixed value of $\beta = 2.0$, which is indexed to the dust opacity κ_0. Since the 70 μm flux value likely includes a contribution from a warmer dust component (Casey 2012), we treated it as an upper limit in our MBB fits. For consistency, we did not include any 100 μm flux values in the MBB fits, since observations have not been done to match the depth of our 70 and 160 μm data. We estimated the uncertainties in the fit parameters by running 500 Monte Carlo MBB fits for each set of fluxes, which we let vary randomly within the associated uncertainties for each run. Figures 5 and 6 show the global and disk MBB fits, respectively, with the disk MBB fits shown for fluxes both before and after application of the CLEAN algorithm. The MBB fit parameters and the uncertainties estimated with the Monte Carlo method are listed in Table 5.

We also tried fitting the circumgalactic flux values to the same single MBB, but these fits produced unphysical results (e.g. unrealistically high dust masses). We believe this is due to the faint flux of the circumgalactic emission and the heterogeneous nature of this emission (e.g. filaments of different temperatures and masses). Due to these unphysical results, we calculated a circumgalactic cold dust mass using $M_{cg} = M_{global}$ - M_{disk}. Perhaps a detailed superposition of MBBs could reproduce the combined circumgalactic SED, but that avenue of analysis wades into more degenerate, subjective territory.

5. RESULTS AND DISCUSSION

5.1. Morphology

We find circumgalactic cold dust features for all six of our sample wind galaxies. The most extended features range from 1.2 kpc (NGC 1800) to 2.6 kpc (He 2-10) as measured from the center of the galaxy or from the mid-plane of a disk-like region out to the furthest part of the feature at least 3σ above the background. These features extend to scales of $\sim$1.2-2.5 times the radii of the stellar component as measured by the 4.5 μm stellar disk region, and typically do not trace the orientation of the stellar disk. The circumgalactic features vary in morphology including extended filaments (NGC 1569, NGC 1705, NGC 1800, NGC 3077, and NGC 5253), clouds or knots of dust apparently separated from the disk region (NGC 1569, NGC 1705, and NGC 5253), as well as broader regions extending over large circumgalactic angles (e.g. He 2-10). This varied morphology suggests different processes can lead to the presence of cold dust in circumgalactic regions. As a member of the M81 group, NGC 3077 is in the process of interacting with M81 and M82, so much of the circumgalactic cold dust features must be attributed to tidal stripping. In particular, the features to the east, west and north-northeast of NGC 3077 are most likely due to tidal stripping mostly from M81, since 21 cm observations (Cottrell 1976; van der Hulst 1979; Yun et al. 1994) show H I tidal streams in those regions.

Some cold circumgalactic dust features coincide with similar emission features in the ancillary Hα, 8.0, and 24 μm data (e.g. filaments of NGC 1569 and NGC 1800), but others do not (e.g. the broader plume extending SSW from NGC 1705). Also, the cold circumgalactic features do not always match the morphology of their shorter wavelength counterparts. For example, the cold dust around NGC 1705 exhibits a somewhat filamentary morphology while the Hα features are more shell-like. Therefore, hot and warm wind components like Hα and polycyclic aromatic hydrocarbon (PAH) emission will not correlate exactly with the cold dust component, and should not be used as a predictor of cold dust or vice versa. This result supports the idea of shielded regions within a galactic wind where dust may remain protected from sputtering via thermal, radiation, or collisional processes (Jurac et al. 1998; Gnedin & Draine 2014). Appendix A contains further discussion of individual galaxies, their cold dust features, and comparisons with H I and X-ray observations.

5.2. 70μm / 160μm Ratio Maps

In order to estimate the dust temperature and its spatial distribution using a proxy measurement, we made ratio maps of the 70μm to 160μm emission. The dust emissivity, β, and dust grain size distribution can also contribute to variations in 70μm / 160μm values (see Paper I). We first convolved the 70μm maps to the pixel scale of the 160μm maps using the convolution kernels described in Aniano et al. (2011). We then aligned the resulting convolved images with the 160 μm maps and took the ratio, limiting the plotted ratios to pixels where the 160 μm map had values >0.0001 Jy/pixel ($\sim 1\sigma$ above the background) for the sake of clearly displaying galactic features. The 70μm / 160μm ratio maps are shown in Figure 7. All of the galaxies exhibit warmer dust temperatures (ratio >1.0) near their nuclei as would be expected for the stronger radiation field in nuclear regions, while their outer regions tend to appear cooler. Unlike the rest of the galaxies, NGC 3077 has a striking temperature gradient along the northeast to southwest axis. The cooler dust to the southwest of the nucleus appears to coincide with warm dust in the 8.0 and 24 μm maps, and the H I tidal stream towards M81 (Cottrell 1976; van der Hulst 1979; Yun et al. 1994), but not any obvious Hα feature. The warmer regions in the ratio maps shown by yellow and red colors in Figure 7 do not appear to correlate well in a qualitative sense with much of the warm dust features in the 8.0 and 24 μm maps or hot ionized gas of the Hα maps, though some exceptions arise like the bright filament to the southwest of NGC 1569 and the warmer region to the east of the nucleus in NGC 5253 coinciding with the ionization cone reported by Zastrow et al. (2011). The temperature structure of He 2-10 exhibits a more disturbed temperature distribution than the other galaxies. At least three distinct warmer regions outside the nucleus extend in twisting filaments rather than a smooth gradient, perhaps due to anisotropic heating via AGN activity in its nucleus (Reines et al. 2011).

5.3. Comparing Dust and Host Galaxy Properties

Table 5 lists the cold dust masses and temperatures of each galaxy fit via MBB for both the global and disk regions. The fit global cold dust masses are in the range $\sim 10^5$ - $10^{6.5}$ $M_\odot$. To estimate gas masses (M_{gas}) of the galaxies in our sample, we first found a star formation rate (via Kennicutt 1998) from the total IR luminosity (L_{IR}) in Table 1 and then used this value to find a gas surface density by inverting the composite Kennicutt-Schmidt law as in Tremonti et al. (2004) (adjusting for He):

$$\Sigma_{SFR} = 1.6 \times 10^{-4} \left(\frac{\Sigma_{gas}}{1 M_\odot \ pc^{-2}} \right)^{1.4} M_\odot \ yr^{-1} \ kpc^{-2} \tag{2}$$

With the caveat that the gas masses found via this method may be very uncertain, the values we find are in the range $\sim 10^{7.5}$ - 10^9 $M_\odot$. Comparing these with the respective global dust masses, we estimate gas-to-dust ratios of $\sim$ 115 for NGC 1800 and NGC 3077 (fairly consistent with the Milky Way ratio of $\sim$ 140 (see Table 2 in Draine et al. 2007), while the remaining galaxies in our sample appear to be relatively dust poor with gas-to-dust ratios of $\sim$ 240-330.

We calculated the circumgalactic cold dust mass (M_{cg}) shown in Table 5 by subtracting the disk cold dust mass (M_{disk}) from the global cold dust mass (M_{global}). Figure 8 shows M_{cg} versus the total baryonic (stellar plus gas) mass for the galaxies in our sample. The stellar masses (M_*) are listed in Table 1 and were calculated using the same method as Zastrow et al. (2013) (see Table 1 for more detail). The power law fit $M_{cg} = (M_* + M_{gas})^\alpha$ has an exponential dependence with $\alpha = 1.35 \pm 0.25$, suggesting the circumgalactic dust which likely manifests from megayear timescale processes still correlates with the baryonic mass which has evolved on gigayear timescales. In Figure 9, we show M_{cg} normalized by M_{global} versus star formation rate surface density (Σ_{SFR}) using the star formation rate as calculated above together with the extent of the Hα emission ($R_{H\alpha}$) listed in Table 1 of Calzetti et al. (2010). We did not correct for possible AGN contributions to the FIR emission in He 2-10, so its dust masses and star formation values carry that caveat, indicated by the open red circle for He 2-10 in Figures 8-12. Although the typical dust mass uncertainties from the MBB fitting are on the order of $\sim$ 40%, Figure 9 still shows $\sim$10-30% of the cold dust in most of these wind-hosting dwarf galaxies can be found in the circumgalactic region, with NGC 1569 having $\sim$70% of its cold dust in the circumgalactic region. NGC 3077 must be considered a bit of an outlier due to the potential dust contribution from tidal streams due to interaction with M81 and M82. These data also hint at a possible positive trend in M_{cg}/M_{global} with Σ_{SFR}, but the uncertainties in the dust masses and the very large circumgalactic cold dust fraction for NGC 1569 make the data consistent with no trend as well. Comparing the fit global dust temperature (T_{global}) with Σ_{SFR} (Figure 10) provides stronger evidence for a positive trend, as would be expected from a more luminous ultraviolet (UV) radiation field in higher Σ_{SFR} galaxies. The trend of larger circumgalactic-to-global cold dust fraction with higher Σ_{SFR} hinted at in Figure 9 is supported further in Figure 11, which shows the circumgalactic flux normalized by the global flux versus Σ_{SFR} for the PACS and SPIRE bands. Note how the flux fraction trend with Σ_{SFR} progresses from negative at 70 μm to positive at 500 μm.

Given the large fraction of circumgalactic dust around the tidally disturbed NGC 3077, it is natural to ask whether the immediate intergalactic environment plays an important role in stirring up this circumgalactic dust. Karachentsev & Makarov (1999) developed a tidal index parameter (Θ_i) as a measure of the galaxy's interaction based on a combination of the three-dimensional distance and masses of its nearest neighbors. The maximum value of Θ_i determines the galaxy's "Main Disturber" (MD). A maximum Θ_i greater than zero indicates gravitational interaction with the MD within a tidal radius, while a value less than zero indicates a relatively isolated galaxy outside that tidal radius. Amongst our sample, NGC 1569, NGC 3077, and NGC 5253 have positive Θ_i values (Karachentsev et al. 2014), of which NGC 3077 unsurprisingly has the highest value. He 2-10, NGC 1705, and NGC 1800 all have negative Θ_i values indicating their isolation, so it becomes challenging to explain their circumgalactic dust by way of tidal disturbance. In the case of NGC 3077, there is likely a combination of tidal dust streams and dust lifted into the halo via star formation, accounting for its larger fraction of circumgalactic dust.

If a galaxy's dust carries fractionally more metals than its gas, infall addition or outflow removal of dust to or from the galaxy's ISM can significantly affect the overall metallicity (Spitoni et al. 2010), though some controversy over these scenarios remains (Feldmann 2015). We determined a metallicity (12 + log(O/H)) for each galaxy in our sample using the emission line method developed in Pettini & Pagel (2004) (using ([O III]/Hβ)/(N II/Hα)) with emission line strengths from a few sources (see Table 1). In order to compare these metallicities with the mass-metallicity relation derived in Tremonti et al. (2004), we used the metallicity calibration conversion found in Kewley & Ellison (2008) to calculate analogous values, taking into account the $\sim$0.1 dex uncertainty in the Pettini & Pagel (2004) method as well as the $\sim$0.06 dex uncertainty in the conversion (Kewley & Ellison 2008). The converted values are listed in Table 1. The mass-metallicity relation derived in Tremonti et al. (2004)

is:

$$12 + \log(O/H) \;=\; -\,1.492 + 1.847(\log M_*) - 0.08026(\log M_*)^2 \qquad (3)$$

where O/H is the oxygen abundance and M_* is the stellar mass in units of solar masses. The equation is valid over the mass range $8.5 < \log\, M_* < 11.5$. We used this relation and the M_* values listed in Table 1 to calculate the predicted value of 12 + log(O/H)$_{pre}$. In Figure 12, we calculate a metallicity deficit by subtracting 12 + log(O/H)$_{pre}$ from the value derived from emission line strengths (Δ log(O/H)) and compare that to M_{cg}/M_{global}. In NGC 3077 and He 2-10, dusty tidal streams and AGN should be considered respectively when interpreting Figure 12. The tidal streams of NGC 3077 likely increase M_{cg}/M_{global}, even though our observations do not cover the entire spatial extent of the streams when compared with the H I data (Cottrell 1976; van der Hulst 1979; Yun et al. 1994). The AGN in He 2-10 (Reines et al. 2011) may eject and heat dust more efficiently, thus increasing M_{cg}/M_{global}. Also, log(O/H) can be overestimated in the presence of an AGN, which will contribute to [O III]/Hβ. With these considerations for NGC 3077 and He 2-10 in mind, Figure 12 hints at an upward trend of M_{cg}/M_{global} with larger O/H deficits. However, the uncertainties in both Δ log(O/H) and M_{cg}/M_{global} and the small number statistics preclude any statistically significant conclusions.

6. SUMMARY

In this second paper of a series (see Paper I), we have utilized new, very deep *Herschel Space Observatory* data of six nearby dwarf galaxies with known galactic-scale winds to investigate the detailed structure and properties of cold dust. *Herschel's* gains in resolution and light-collecting ability over earlier instruments (e.g. *Spitzer* MIPS) allowed us to resolve and detect previously unavailable details. Spatial decomposition of circumgalactic and disk regions has allowed us to investigate the properties of cold dust found outside the disk. Our analysis of these observations has yielded the following results:

- *Detection and kiloparsec-scale extent of cold dust features.* We detected circumgalactic cold dust features in all six of our sample of nearby dwarf galaxies with known galactic-scale winds. These features range in maximum extent from 1.2-2.6 kpc and are similar in scale to their host galaxy's stellar radii, but typically do not trace the stellar component.

- *Varied morphology.* We identified cold dust features with filamentary structure, dust clouds distinct from their host galaxies, and broad angle regions with more uniform emission distribution.

- *Imperfect spatial correlation with other wind components.* Some cold dust features we identified coincide with similar emission features in Hα, 8.0, and 24 μm data, but others do not, preventing the simple prediction of one component via another.

- *Significant fraction of the total dust mass found outside the stellar disk.* Through the spatial decomposition of circumgalactic and disk regions, we found that a substantial ~10-30% of the total dust mass resides in the circumgalactic region. In the case of NGC 1569, this value is ~70%.

- *Tantalizing correlations between dust properties and Σ_{SFR}.* Comparisons of circumgalactic cold dust mass fraction and global dust temperature with star formation rate surface density suggest potential positive correlations, but the uncertainties in dust mass and temperature as well as small number statistics make these conclusions tenuous at best.

- *Limited environmental dependence.* The presence of circumgalactic cold dust features for our dwarf galaxies doesn't obviously depend on the gravitational influence of neighboring galaxies, though it may play a role for certain sources.

- *A hint towards metallicity depletion via cold dust outflow.* Comparing the fraction of circumgalactic cold dust mass with galaxy metallicity points towards a greater metallicity deficit in those galaxies with fractionally more circumgalactic dust, but uncertainties in the dust mass and metallicity plus small number statistics preclude any solid conclusion.

ACKNOWLEDGEMENTS

This work is based in part on observations made with *Herschel*, which is an ESA space observatory with science instruments provided by European-led Principle Investigator consortia and with important participation from NASA. Support for this work was provided by NASA through *Herschel* contracts 1427277 and 1454738 (AM, SV, and MM). We thank Hélène Roussel for her guidance in using the *Scanamorphos* software and Peter Teuben for his help converting old Hα data. This work has made use of NASAs Astrophysics Data System Abstract Service and the NASA/IPAC Extragalactic Database (NED), which is operated by the Jet Propulsion Laboratory, California Institute of Technology, under contract with the

National Aeronautics and Space Administration. PACS has been developed by a consortium of institutes led by MPE (Germany) and including UVIE (Austria); KU Leuven, CSL, IMEC (Belgium); CEA, LAM (France); MPIA (Germany); INAF-IFSI/OAA/OAP/OAT, LENS, SISSA (Italy); IAC (Spain). This development has been supported by the funding agencies BMVIT (Austria), ESA-PRODEX (Belgium), CEA/CNES (France), DLR (Germany), ASI/INAF (Italy), and CICYT/MCYT (Spain). SPIRE has been developed by a consortium of institutes led by Cardiff University (UK) and including Univ. Lethbridge (Canada); NAOC (China); CEA, LAM (France); IFSI, Univ. Padua (Italy); IAC (Spain); Stockholm Observatory (Sweden); Imperial College London, RAL, UCL-MSSL, UKATC, Univ. Sussex (UK); and Caltech, JPL, NHSC, Univ. Colorado (USA). This development has been supported by national funding agencies: CSA (Canada); NAOC (China); CEA, CNES, CNRS (France); ASI (Italy); MCINN (Spain); SNSB (Sweden); STFC, UKSA (UK); and NASA (USA). HIPE is a joint development (are joint developments) by the Herschel Science Ground Segment Consortium, consisting of ESA, the NASA Herschel Science Center, and the HIFI, PACS and SPIRE consortia.

A. NOTES ON INDIVIDUAL GALAXIES

- *Henize 2-10* - Broad cold dust emission regions surround He 2-10 out to ~ 1.5 pc in all SPIRE bands as well as the 160 μm PACS map, which appears similar in extent and morphology to the H I distribution observed by Kobulnicky et al. (1995). The 70 μm PACS map exhibits a bit more anisotropy in its distribution of circumgalactic emission with tapering features extending to the north-northeast, southwest, and east-southeast. The nort-northeast tapering feature extends furthest to ~ 2.6 kpc. The orientation of these tapering features appears similar to the smaller 0.5 kpc-scale Hα bubbles (Méndez et al. 1999; Zastrow et al. 2013), but appears less correlated with the shape of the X-ray emission (Kobulnicky & Martin 2010). Several knots of emission separated from He 2-10 by $\sim$3-4 kpc to the northwest and southwest in the PACS maps cannot be definitively ruled out as background sources given the signal to noise levels or foreground Milky Way dust clouds, but coincident emission in the SPIRE maps seems connected to the disk via colder streams bridging their separation. The most prominent emission in the SPIRE maps towards the knots northwest of the disk seems similarly oriented to an X-ray feature observed by Kobulnicky & Martin (2010).

- *NGC 1569* - A dense complex of filamentary and broad circumgalactic cold dust features stretch out from all along the disk of NGC 1569. The prominent Hα, 8.0, and 24 μm filament (Waller 1991; Hunter et al. 1993; Westmoquette et al. 2008; McCormick et al. 2013) extending southwest from the western edge of the disk also shows up in the PACS maps, but becomes fainter and disappears in the SPIRE bands. A clump of cold dust directly south of the galactic nucleus resides $\sim$1.8 kpc from the disk midplane and appears to have made a clean break with the other circumgalactic cold dust emission in the PACS maps. Some faint 8.0 μm emission (McCormick et al. 2013) coincides with this rogue clump and some extended X-ray emission (Heckman et al. 1995; della Ceca et al. 1996) may as well. The rogue clump has no obvious counterpart in Hα emission, but supershell features surrounding its location (Martin 1998; Westmoquette et al. 2008) suggest it resides at the center of a ionized gas shell. The structure of the rogue clump suggests anisotropic heating with the warmer 70 μm emission closer to the galactic disk and the colder emission in the SPIRE maps extending further away. The bright emission to the southwest corner of the SPIRE maps comes from foreground Milky Way cirrus.

- *NGC 1705* - Vertical filamentary cold dust emission to the north and south of NGC 1705 coincides with the H I emission, which Meurer et al. (1998) has shown consists mainly of a rotating disk. However, Meurer et al. also note an H I "spur" which is kinematically distinct from the the rotating disk and spatially consistent with the

Hα outflow (Meurer et al. 1989, 1992; Zastrow et al. 2013). Our PACS maps show evidence of a similarly consistent cold dust feature extending almost exactly north from the galaxy. Also in the PACS maps, two bright knots of emission directly to the south are separated from the galactic center by $\sim$1.3 and 1.5 kpc respectively. These knots are also approximately coincident with the rotating H I disk, also appear in the SPIRE maps, and do not have associated background sources. North-northeast of the nucleus, a bright cloud of cold dust appears as a knot in the 70 μm PACS map but has broader spatial extent in our other four *Herschel* maps. This cloud with no obviously associated background source seems spatially consistent with the orientation of the northern Hα superbubble (Zastrow et al. 2013), but resides well beyond its edge ($>$0.5 kpc), making it a likely example of material swept out of the ISM by an expanding superbubble (Heckman et al. 2001). However, we did not include this cloud in the global flux measurements, since it cannot be definitively ruled out as a background source.

- *NGC 1800* - An C-shaped filament of circumgalactic cold dust extends from the northwestern edge of NGC 1800 to $\sim$1.2 kpc north of the disk in the 70 μm PACS map tracing a similar feature in 8.0 μm emission. In addition there is some more diffuse, less bright 70 μm emission above the disk to the east of this filament. These features lie just south of the filamentary web of Hα emission (Hunter et al. 1994; Marlowe et al. 1995; Hunter 1996). The cold dust features along the northwestern edge of NGC 1800 are offset from the Hα "fingers" of Hunter (1996), which extend from the the northeastern edge of the disk. An offset also exists between the southern edge cold dust features which appear like two broad nubs splayed out from the eastern and western edges of the disk in our SPIRE maps versus the centrally concentrated Hα "fingers" and shell outside the disk (again from Hunter 1996). Observations by Rasmussen et al. (2004) reveal X-ray emission crossing the disk of NGC 1800 approximately from southeast to northwest at an angle with respect to the stellar component. The northern extent of this hot X-ray gas above the disk appears to coincide with some of the emission from cold dust in the PACS maps. Within the galactic disk, the peak of the dust emission is offset to the west from the stellar component, perhaps helping explain why the strongest dust feature - the C-shaped filament extending north - emanates from that part of galaxy. What may appear as cold dust knots to the south in the PACS images could also be either Galactic dust heated by foreground Milky Way stars or emission from background sources evident in the 4.5 μm IRAC map.

- *NGC 3077* - Most if not all of the circumgalactic cold dust features we observe for NGC 3077 can be attributed to the same tidal interaction forces with M81 and M82, which produce tidal arms of H I and the complex of H I and CO offset to the east of the galaxy's stellar component (Cottrell 1976; van der Hulst 1979; Yun et al. 1994; Walter & Heithausen 1999). However, certain cold dust features appear to complement the morphology of the Hα emission (Martin 1998; Calzetti et al. 2004). A C-shaped filament and a knot of cold dust at its tip extending $\sim$2.6 kpc north of the stellar disk reside directly above the location of an Hα shell (Calzetti et al. 2004). A circumferential arc of cold dust visible in the PACS maps and the 250 μm SPIRE map to the south of the disk also traces the edge of a superbubble observed in Hα and X-ray emission (Martin 1998; Ott et al. 2003). Cold dust filaments, clouds, broad regions, and clumps to the east and west of NGC 3077 are likely associated with the H I features (Yun et al. 1994). The argument has been made that the superbubbles of hot plasma and ionized gas have yet to break out of this galaxy but potentially have enough energy to generate a breakout wind in the northern direction where there is less H I density (Ott et al. 2003). The cold dust emission along the north-south direction in the PACS maps appears stronger than the east-west emission while the inverse is true of the east-west emission in the SPIRE maps, which would seem to support the argument for a wind developing in the northern direction.

- *NGC 5253* - The morphology of the circumgalactic cold dust features in our PACS and SPIRE maps appears to follow the distribution of H I (Kobulnicky & Skillman 2008) more closely than any other galaxy component. However, features like the broad emission regions extending from the northwest and southeast edges of the stellar disk in the *Herschel* maps do follow ionized gas features (Marlowe et al. 1995; Calzetti et al. 1999; Zastrow et al. 2011), X-ray emission (Strickland & Stevens 1999), and some 8.0 μm features (McCormick et al. 2013). Filaments extend south in the 70, 160, and 250 μm maps, where the westernmost filament protruding from the southwest edge of the disk extends at least $\sim$2 kpc from the disk. In the PACS maps, a circumgalactic cold dust filament also extends directly north from the disk. Looking along the north-south direction, the 500 μm SPIRE map shows tenuous evidence for a significantly larger scale bipolar filamentary emission extending to $\sim$5 kpc outside the galactic disk. The southern extent of this emission appears disturbed and perhaps coincides with the H I plume interpreted by Kobulnicky & Skillman (2008) as a potential outflow or inflow. However, no obvious counterpart for the northern filament presents itself in the H I images. The challenge of ruling out background sources or cold Milky Way dust clouds remains a concern for this north-south emission, but the brightest features from apparent clouds within this structure are $>4\sigma$ above the background in the 500 μm SPIRE map.

REFERENCES

Aalto, S., Garcia-Burillo, S., Muller, S., et al. 2012, A&A, 537, A44

Alatalo, K., Blitz, L., Young, L. M., et al. 2011, ApJ, 735, 88

Aniano, G., Draine, B. T., Gordon, K. D., & Sandstrom, K. 2011, PASP, 123, 1218

Bell, E. F., McIntosh, D. H., Katz, N., & Weinberg, M. D. 2003, ApJS, 149, 289

Bolatto, A. D., Warren, S. R., Leroy, A. K., et al. 2013, Nature, 499, 450

Buote, D. A. 2000, ApJ, 539, 172

Calzetti, D., Conselice, C. J., Gallagher, J. S., III, & Kinney, A. L. 1999, AJ, 118, 797

Calzetti, D., Harris, J., Gallagher, J. S., III, et al. 2004, AJ, 127, 1405

Calzetti, D., Wu, S.-Y., Hong, S., et al. 2010, ApJ, 714, 1256

Casey, C. M. 2012, MNRAS, 425, 3094

Cicone, C., Maiolino, R., Sturm, E., et al. 2014, A&A, 562, AA21

Cottrell, G. A. 1976, MNRAS, 174, 455

Dalcanton, J. J., Williams, B. F., Seth, A. C., et al. 2009, ApJS, 183, 67

Dale, D. A., Cohen, S. A., Johnson, L. C., et al. 2009, ApJ, 703, 517

de Vaucouleurs, G., de Vaucouleurs, A., Corwin, H. G., Jr., et al. 1991, Third Reference Catalogue of Bright Galaxies (New York, NY: Springer)

della Ceca, R., Griffiths, R. E., Heckman, T. M., & MacKenty, J. W. 1996, ApJ, 469, 662

Di Matteo, T., Springel, V., & Hernquist, L. 2005, Nature, 433, 604

Draine, B. T. 2003, ARA&A, 41, 241

Draine, B. T., Dale, D. A., Bendo, G., et al. 2007, ApJ, 663, 866

Ehle, M., Dahlem, M., Jiménez Bailón, E., Santos-Lleó, M., & Read, A. M. 2004, IAU Symp. 217, Recycling Intergalactic and Interstellar Medium, held in Syndey, Australia, Ed P.-A. Duc J. Braine and E. Brinks, San Francisco: ASP, 154

Engelbracht, C. W., Kundurthy, P., Gordon, K. D., et al. 2006, ApJ, 642, L127

Feldmann, R. 2015, MNRAS, 449, 3274

Ferrarese, L., & Merritt, D. 2000, ApJ, 539, L9

Feruglio, C., Maiolino, R., Piconcelli, E., et al. 2010, A&A, 518, L155

Fischer, J., Sturm, E., González-Alfonso, E., et al. 2010, A&A, 518, L41

Gebhardt, K., Bender, R., Bower, G., et al. 2000, ApJ, 539, L13

Gnedin, N. Y., & Draine, B. T. 2014, ApJ, 795, 37

Griffin, M. J., Abergel, A., Abreu, A., et al. 2010, A&A, 518, L3

Grocholski, A. J., Aloisi, A., van der Marel, R. P., et al. 2008, ApJ, 686, L79

Heckman, T. M., Armus, L., & Miley, G. K. 1990, ApJS, 74, 833

Heckman, T. M., Dahlem, M., Lehnert, M. D., et al. 1995, ApJ, 448, 98

Heckman, T. M., Lehnert, M. D., Strickland, D. K., & Armus, L. 2000, ApJS, 129, 493

Heckman, T. M., Sembach, K. R., Meurer, G. R., et al. 2001, ApJ, 554, 1021

Högbom, J. A. 1974, A&AS, 15, 417

Hopkins, P. F., & Elvis, M. 2010, MNRAS, 401, 7

Hunter, D. A., Hawley, W. N., & Gallagher, J. S., III 1993, AJ, 106, 1797

Hunter, D. A., van Woerden, H., & Gallagher, J. S., III 1994, ApJS, 91, 79
Hunter, D. A. 1996, ApJ, 457, 671
Huo, Z. Y., Xia, X. Y., Xue, S. J., Mao, S., & Deng, Z. G. 2004, ApJ, 611, 208
Irwin, J. A., Wilson, C. D., Wiegert, T., et al. 2011, MNRAS, 410, 1423
Johnson, K. E., Leitherer, C., Vacca, W. D., & Conti, P. S. 2000, AJ, 120, 1273
Jurac, S., Johnson, R. E., & Donn, B. 1998, ApJ, 503, 247
Karachentsev, I. D., Kaisina, E. I., & Makarov, D. I. 2014, AJ, 147, 13
Karachentsev, I. D., & Makarov, D. I. 1999, Galaxy Interactions at Low and High Redshift, 186, 109
Kennicutt, R. C., Jr. 1998, ApJ, 498, 541
Kewley, L. J., & Ellison, S. L. 2008, ApJ, 681, 1183
Kobulnicky, H. A., Dickey, J. M., Sargent, A. I., Hogg, D. E., & Conti, P. S. 1995, AJ, 110, 116
Kobulnicky, H. A., Kennicutt, R. C., Jr., & Pizagno, J. L. 1999, ApJ, 514, 544
Kobulnicky, H. A., & Martin, C. L. 2010, ApJ, 718, 724
Kobulnicky, H. A., & Skillman, E. D. 2008, AJ, 135, 527
Lehnert, M. D., & Heckman, T. M. 1995, ApJS, 97, 89
Lowenthal, J. D., Koo, D. C., Guzman, R., et al. 1997, ApJ, 481, 673
Makovoz, D., & Khan, I. 2005, Astronomical Data Analysis Software and Systems XIV, 347, 81
Marble, A. R., Engelbracht, C. W., van Zee, L., et al. 2010, ApJ, 715, 506
Marlowe, A. T., Heckman, T. M., Wyse, R. F. G., & Schommer, R. 1995, ApJ, 438, 563
Martin, C. L. 1997, ApJ, 491, 561
Martin, C. L. 1998, ApJ, 506, 222
Martin, C. L. 2005, ApJ, 621, 227
Martin, C. L., & Kennicutt, R. C., Jr. 1995, ApJ, 447, 171
McCormick, A., Veilleux, S., & Rupke, D. S. N. 2013, ApJ, 774, 126
McDowell, J. C., Clements, D. L., Lamb, S. A., et al. 2003, ApJ, 591, 154
McQuade, K., Calzetti, D., & Kinney, A. L. 1995, ApJS, 97, 331
Meléndez, M., Veilleux, S., Martin, C., et al. 2015, ApJ, 804, 46
Méndez, D. I., Esteban, C., Filipović , M. D., et al. 1999, A&A, 349, 801
Meurer, G. R., Freeman, K. C., & Dopita, M. A. 1989, Ap&SS, 156, 141
Meurer, G. R., Freeman, K. C., Dopita, M. A., & Cacciari, C. 1992, AJ, 103, 60
Meurer, G. R., Staveley-Smith, L., & Killeen, N. E. B. 1998, MNRAS, 300, 705
Moshir, M., Kopan, G., Conrow, T., et al. 1990, BAAS, 22, 1325
Moustakas, J., & Kennicutt, R. C., Jr. 2006, ApJS, 164, 81
Moustakas, J., Kennicutt, R. C., Jr., Tremonti, C. A., et al. 2010, ApJS, 190, 233
Narayanan, D., Cox, T. J., Kelly, B., et al. 2008, ApJS, 176, 331
Ott, J., Martin, C. L., & Walter, F. 2003, ApJ, 594, 776
Ott, S. 2010, Astronomical Data Analysis Software and Systems XIX, 434, 139
Pettini, M., & Pagel, B. E. J. 2004, MNRAS, 348, L59
Pettini, M., Shapley, A. E., Steidel, C. C., et al. 2001, ApJ, 554, 981
Pietsch, W., Vogler, A., Klein, U., & Zinnecker, H. 2000, A&A, 360, 24

Pilbratt, G. L., Riedinger, J. R., Passvogel, T., et al. 2010, A&A, 518, L1
Poglitsch, A., Waelkens, C., Geis, N., et al. 2010, A&A, 518, L2
Rasmussen, J., Stevens, I. R., & Ponman, T. J. 2004, MNRAS, 354, 259
Read, A. M., Ponman, T. J., & Strickland, D. K. 1997, MNRAS, 286, 626
Reines, A. E., Sivakoff, G. R., Johnson, K. E., & Brogan, C. L. 2011, Nature, 470, 66
Rémy-Ruyer, A., Madden, S. C., Galliano, F., et al. 2014, A&A, 563, A31
Renzini, A. 1997, ApJ, 488, 35
Roussel, H. 2013, PASP, 125, 1126
Roussel, H., Wilson, C. D., Vigroux, L., et al. 2010, A&A, 518, L66
Rupke, D. S., Veilleux, S., & Sanders, D. B. 2002, ApJ, 570, 588
Rupke, D. S., Veilleux, S., & Sanders, D. B. 2005a, ApJS, 160, 87
Rupke, D. S., Veilleux, S., & Sanders, D. B. 2005b, ApJS, 160, 115
Rupke, D. S., Veilleux, S., & Sanders, D. B. 2005c, ApJ, 632, 751
Sakai, S., Ferrarese, L., Kennicutt, R. C., Jr., & Saha, A. 2004, ApJ, 608, 42
Sanders, D. B., Mazzarella, J. M., Kim, D.-C., Surace, J. A., & Soifer, B. T. 2003, AJ, 126, 1607
Sanders, D. B., & Mirabel, I. F. 1996, ARA&A, 34, 749
Schwartz, C. M., & Martin, C. L. 2004, ApJ, 610, 201
Skrutskie, M. F., Cutri, R. M., Stiening, R., et al. 2003, yCat, 7233, 0
Smail, I., Chapman, S. C., Ivison, R. J., et al. 2003, MNRAS, 342, 1185
Smith, M. W. L., Eales, S. A., Gomez, H. L., et al. 2012, ApJ, 756, 40
Spitoni, E., Calura, F., Matteucci, F., & Recchi, S. 2010, A&A, 514, A73
Strickland, D. K., Heckman, T. M., Colbert, E. J. M., Hoopes, C. G., & Weaver, K. A. 2004a, ApJS, 151, 193
Strickland, D. K., Heckman, T. M., Colbert, E. J. M., Hoopes, C. G., & Weaver, K. A. 2004b, ApJ, 606, 829
Strickland, D. K., & Stevens, I. R. 1999, MNRAS, 306, 43
Sturm, E., González-Alfonso, E., Veilleux, S., et al. 2011, ApJ, 733, L16
Tacconi-Garman, L. E., Sturm, E., Lehnert, M., et al. 2005, A&A, 432, 91
Thronson, H. A., Jr., Wilton, C., & Ksir, A. 1991, MNRAS, 252, 543
Tosi, M., Sabbi, E., Bellazzini, M., et al. 2001, AJ, 122, 1271
Tremonti, C. A., Heckman, T. M., Kauffmann, G., et al. 2004, ApJ, 613, 898
Tully, R. B. 1988, Nearby Galaxies Catalog (Cambridge: Cambridge University Press)
van der Hulst, J. M. 1979, A&A, 75, 97
Veilleux, S., Cecil, G., & Bland-Hawthorn, J. 2005, ARA&A, 43, 769
Veilleux, S., Meléndez, M., Sturm, E., et al. 2013, ApJ, 776, 27
Veilleux, S., Rupke, D. S. N., & Swaters, R. 2009, ApJ, 700, L149
Waller, W. H. 1991, ApJ, 370, 144
Walter, F., & Heithausen, A. 1999, ApJ, 519, L69
Weiner, B. J., Coil, A. L., Prochaska, J. X., et al. 2009, ApJ, 692, 187
Westmoquette, M. S., Smith, L. J., & Gallagher, J. S. 2008, MNRAS, 383, 864

Wieprecht, E., Schreiber, J., de Jong, J., et al. 2009, Astronomical Data Analysis Software and Systems XVIII, 411, 531

Yun, M. S., Ho, P. T. P., & Lo, K. Y. 1994, Nature, 372, 530

Zastrow, J., Oey, M. S., Veilleux, S., McDonald, M., & Martin, C. L. 2011, ApJ, 741, L17

Zastrow, J., Oey, M. S., Veilleux, S., & McDonald, M. 2013, ApJ, 779, 76

This preprint was prepared with the AAS LaTeX macros v5.2.

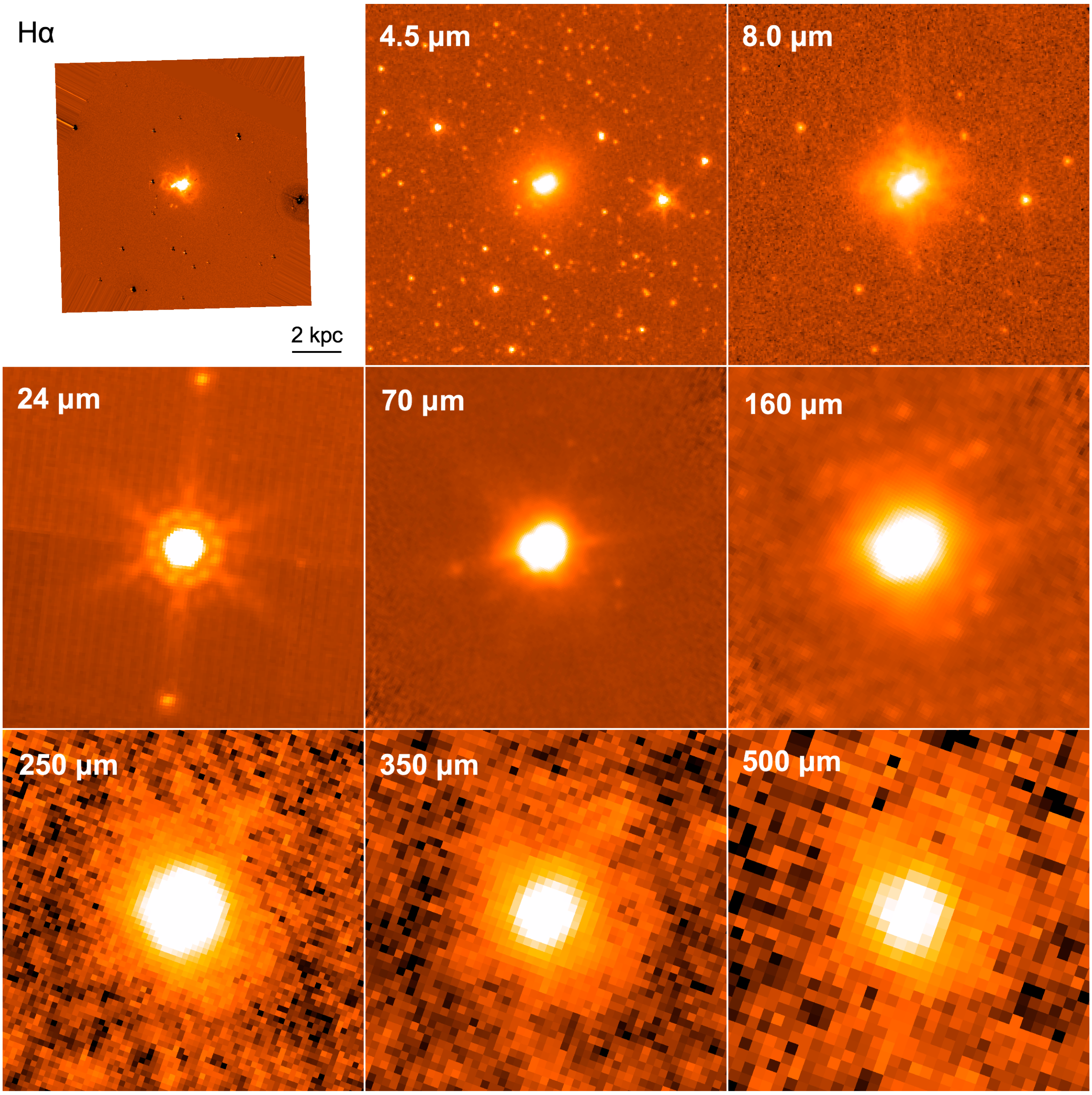

Fig. 1a.— Henize 2-10 - Hα (Zastrow et al. 2013), IRAC 4.5 and 8.0 μm and MIPS 24 μm (*Spitzer* archive, this work), PACS 70 and 160 μm, and SPIRE 250, 350, and 500 μm (this work). All images are displayed with a logarithmic scale. North is up and east is to the left in all images. The bar in the Hα image indicates the scale in all images.

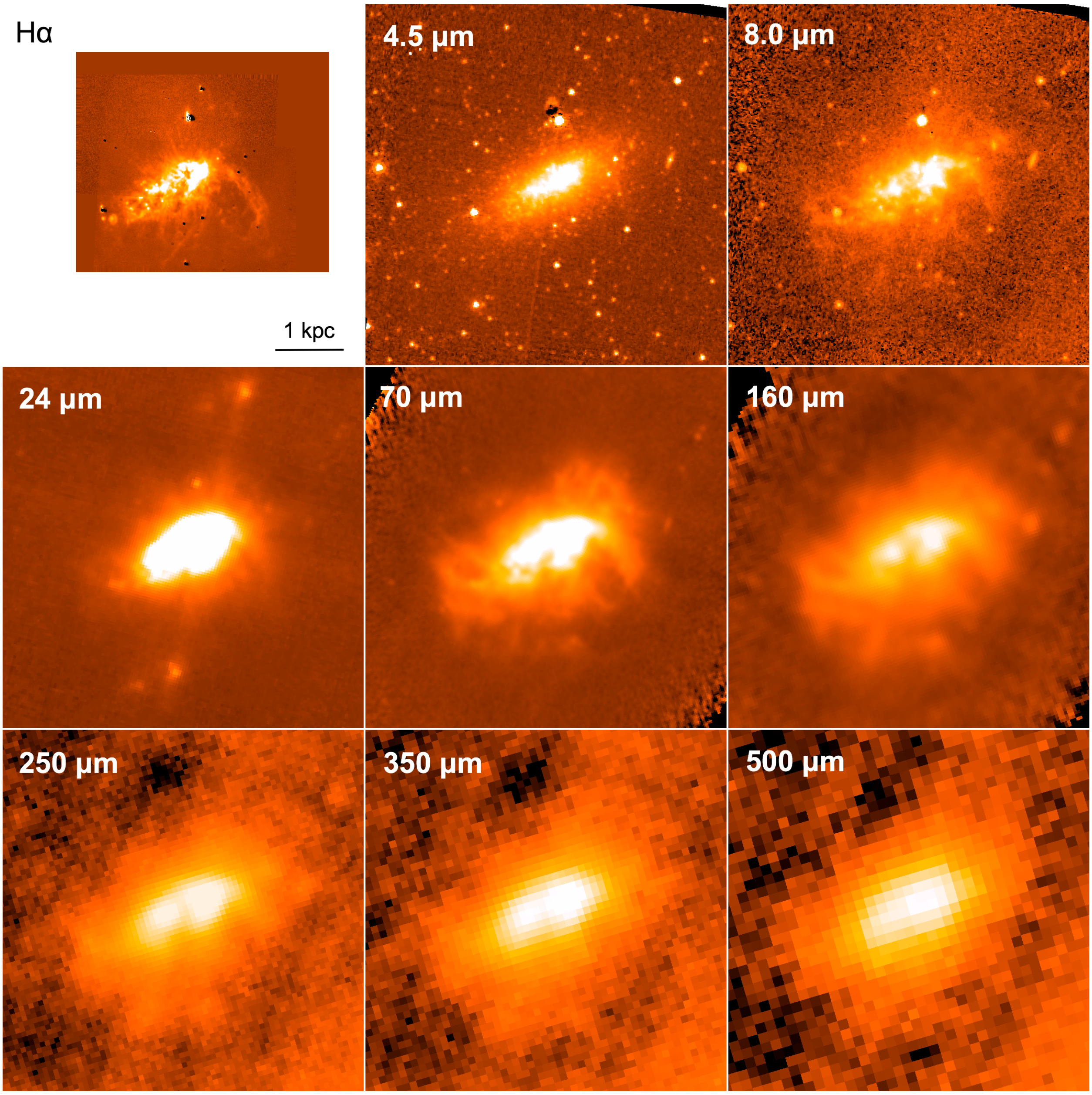

Fig. 1b.— NGC 1569 - Hα (Martin 1997), IRAC 4.5 and 8.0 μm (McCormick et al. 2013), otherwise, the same as in Figure 1a

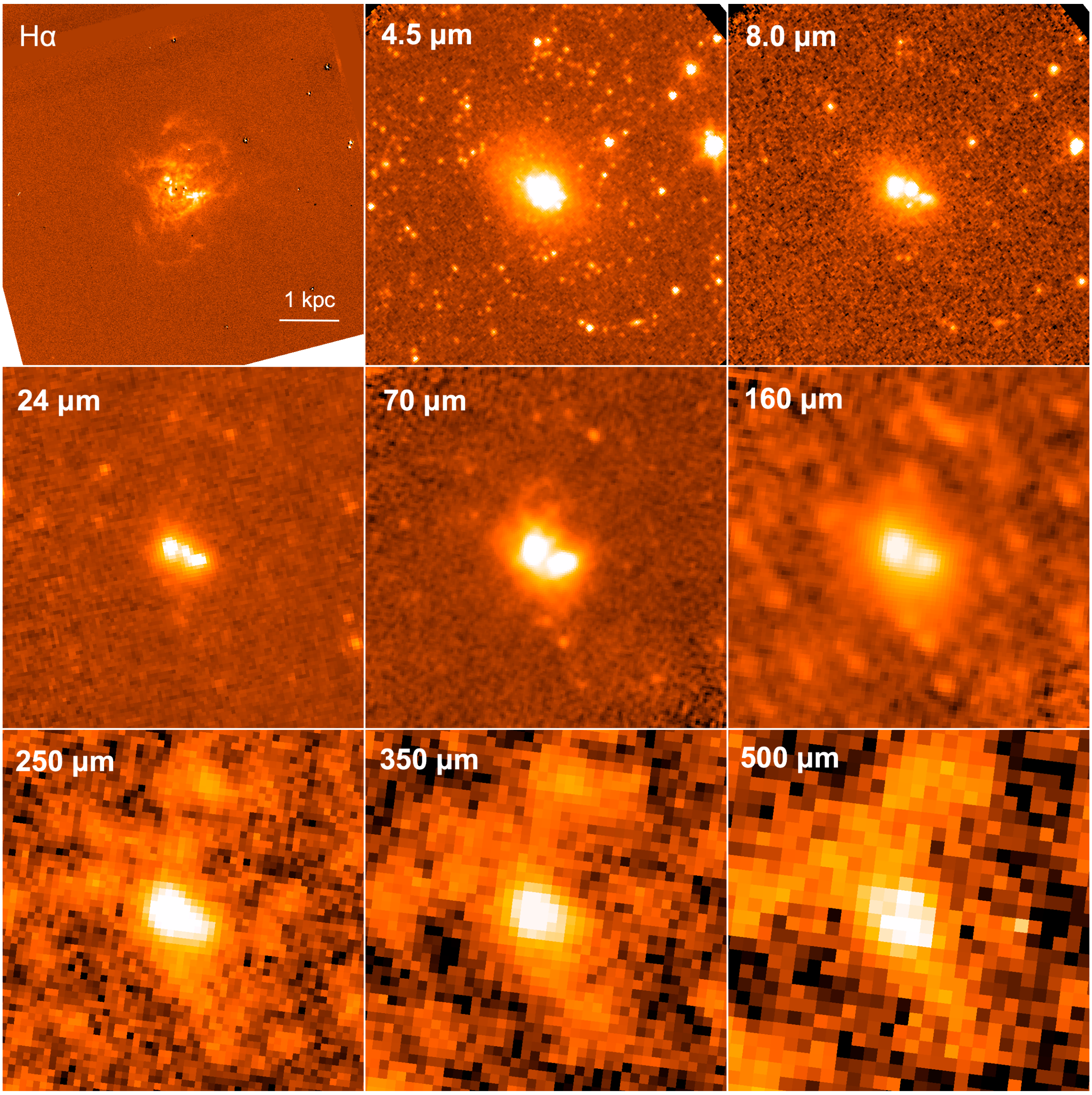

Fig. 1c.— NGC 1705 - Hα (Zastrow et al. 2013), IRAC 4.5 and 8.0 μm (McCormick et al. 2013), otherwise, the same as in Figure 1a

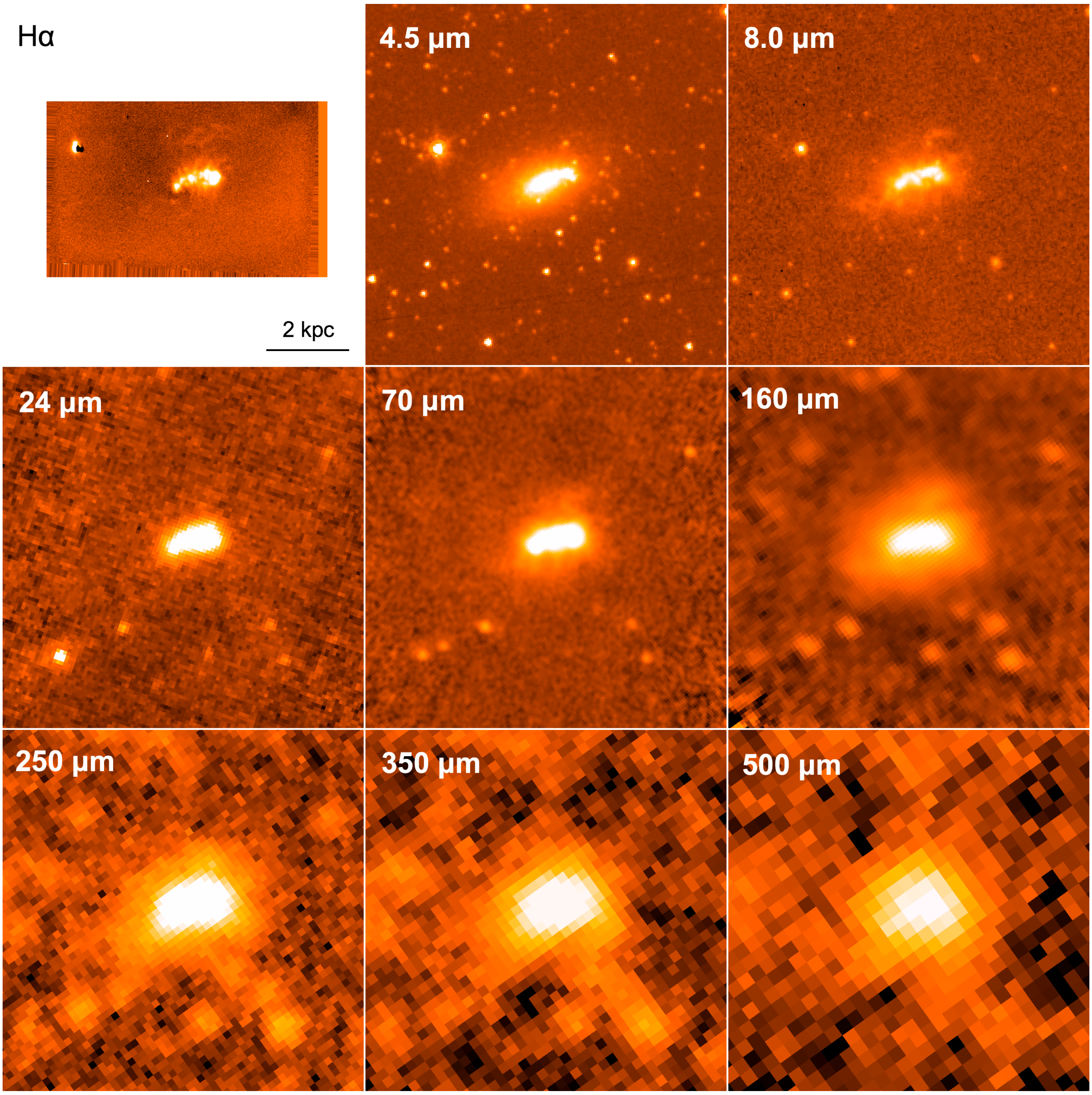

Fig. 1d.— NGC 1800 - Hα data provided by C. Martin, otherwise, the same as in Figure 1a

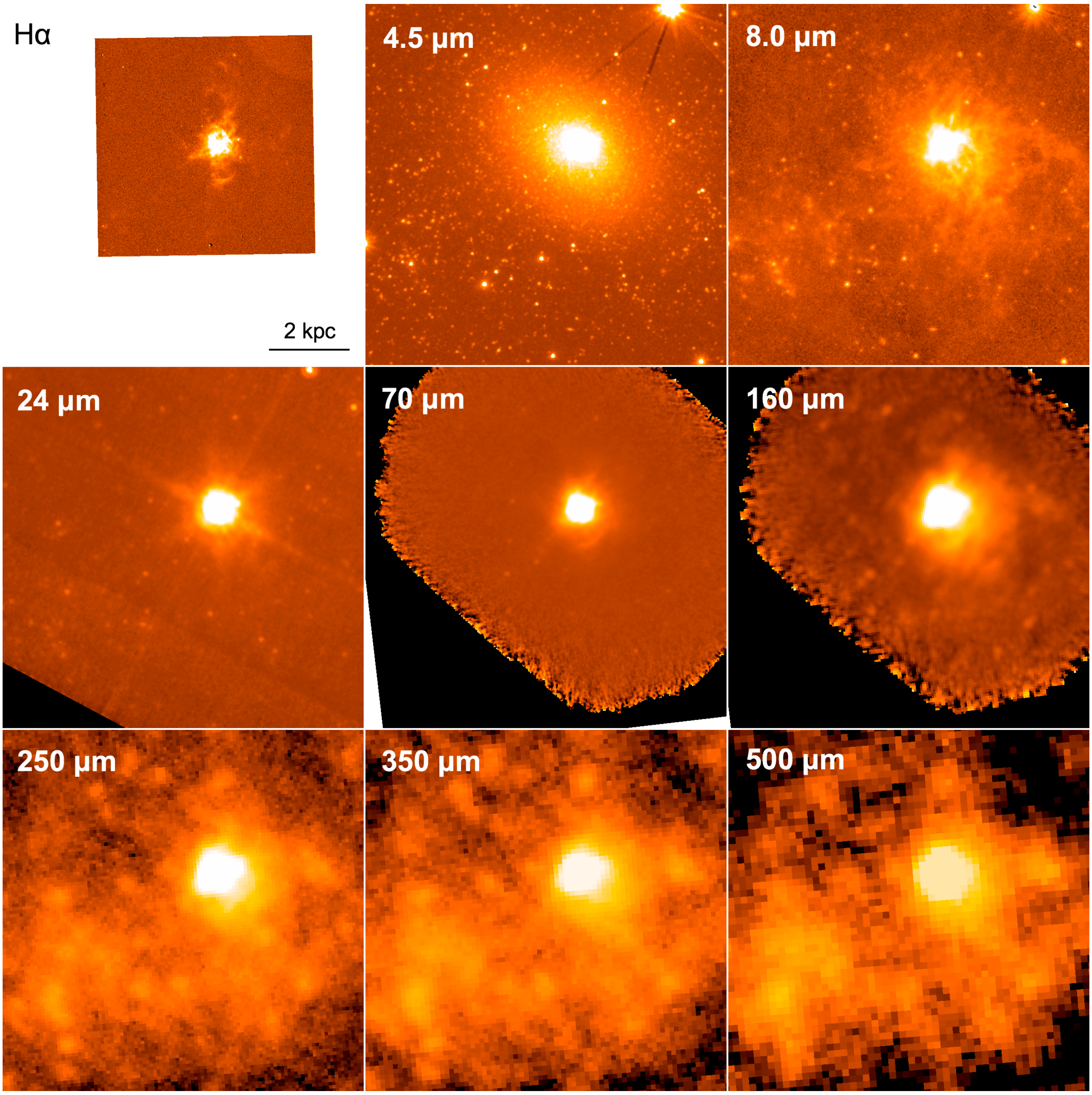

Fig. 1e.— NGC 3077 - Hα (Dale et al. 2009), otherwise, the same as in Figure 1a

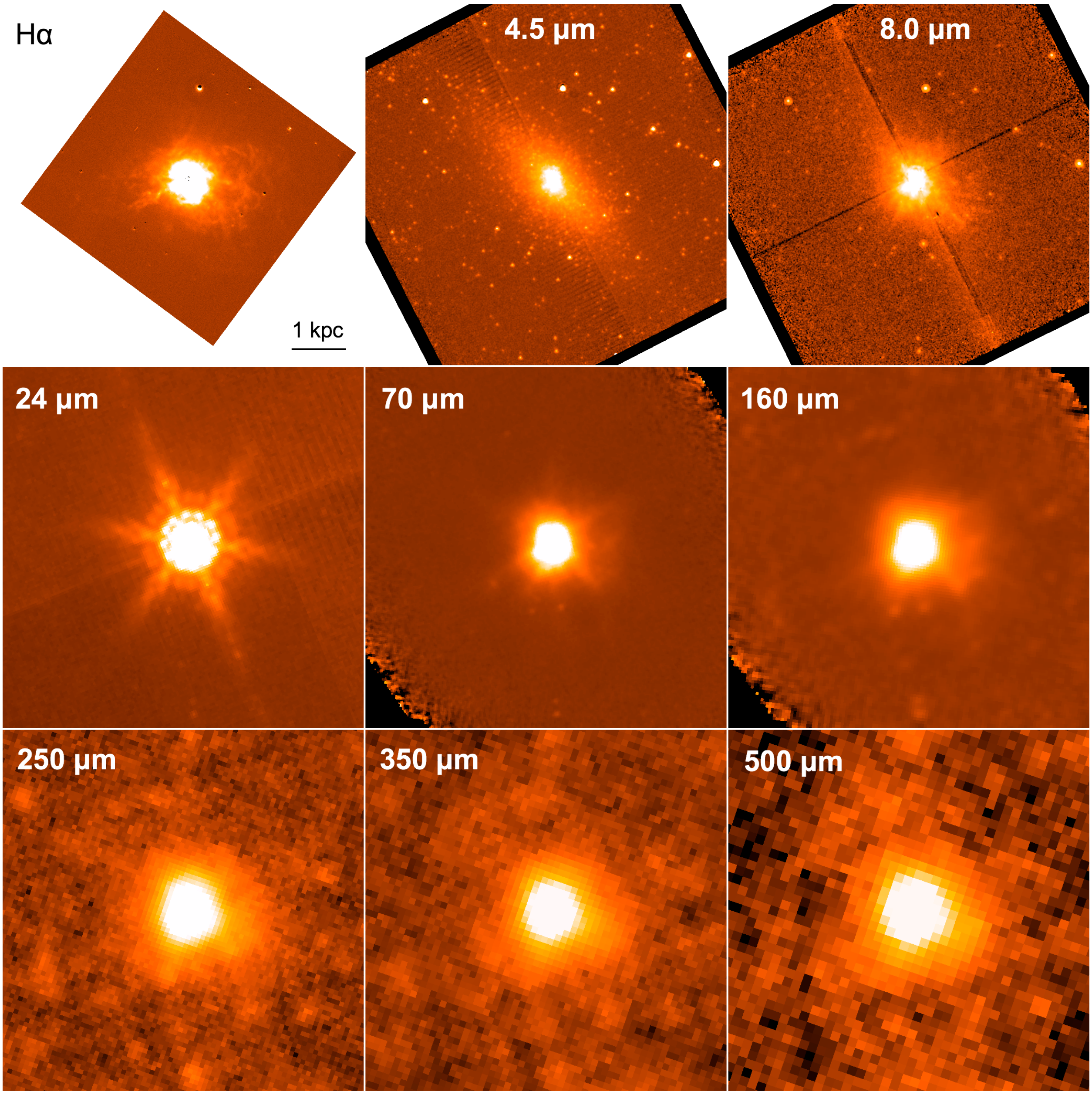

Fig. 1f.— NGC 5253 - Hα (Zastrow et al. 2011), IRAC 4.5 and 8.0 μm (McCormick et al. 2013), otherwise, the same as in Figure 1a

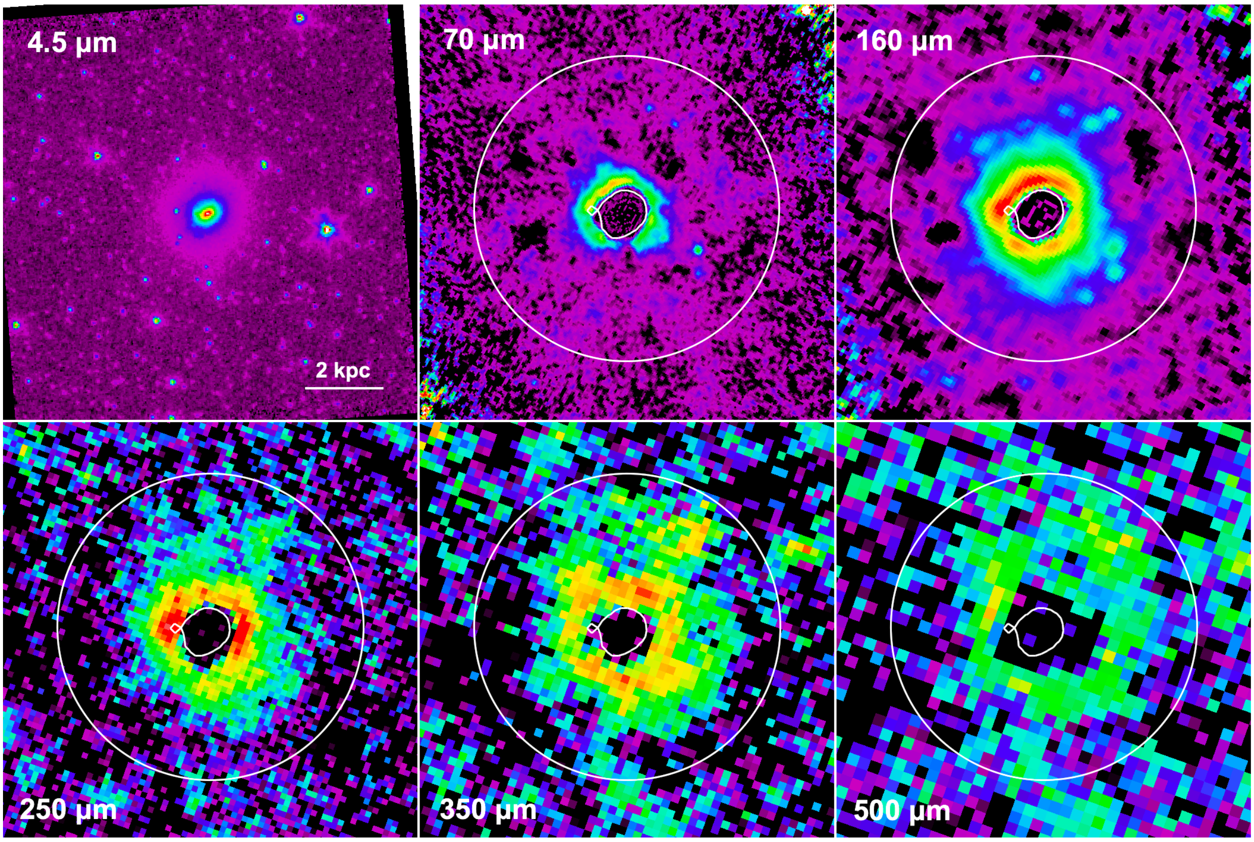

Fig. 2a.— Henize 2-10 - 70, 160, 250, 350, and 500 μm *Herschel* maps after application of our CLEAN algorithm with the IRAC 4.5 μm map for comparison to the stellar component. All images are displayed with a logarithmic scale. North is up and east is to the left in all images. The bar in the 4.5 μm image indicates the scale in all images. The white regions in the *Herschel* maps indicate the global flux region and the stellar disk region derived from the 4.5 μm data.

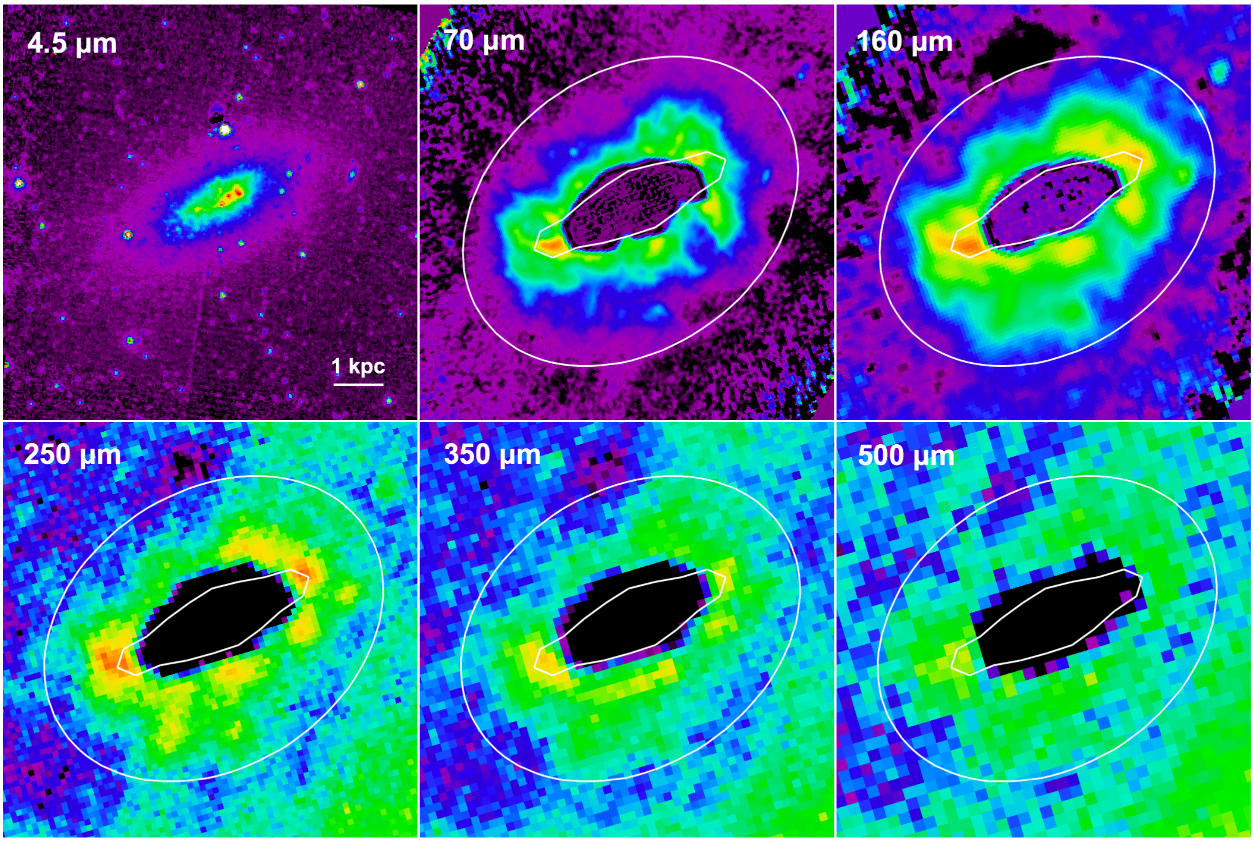

Fig. 2b.— NGC 1569 - display is the same as in Figure 4a

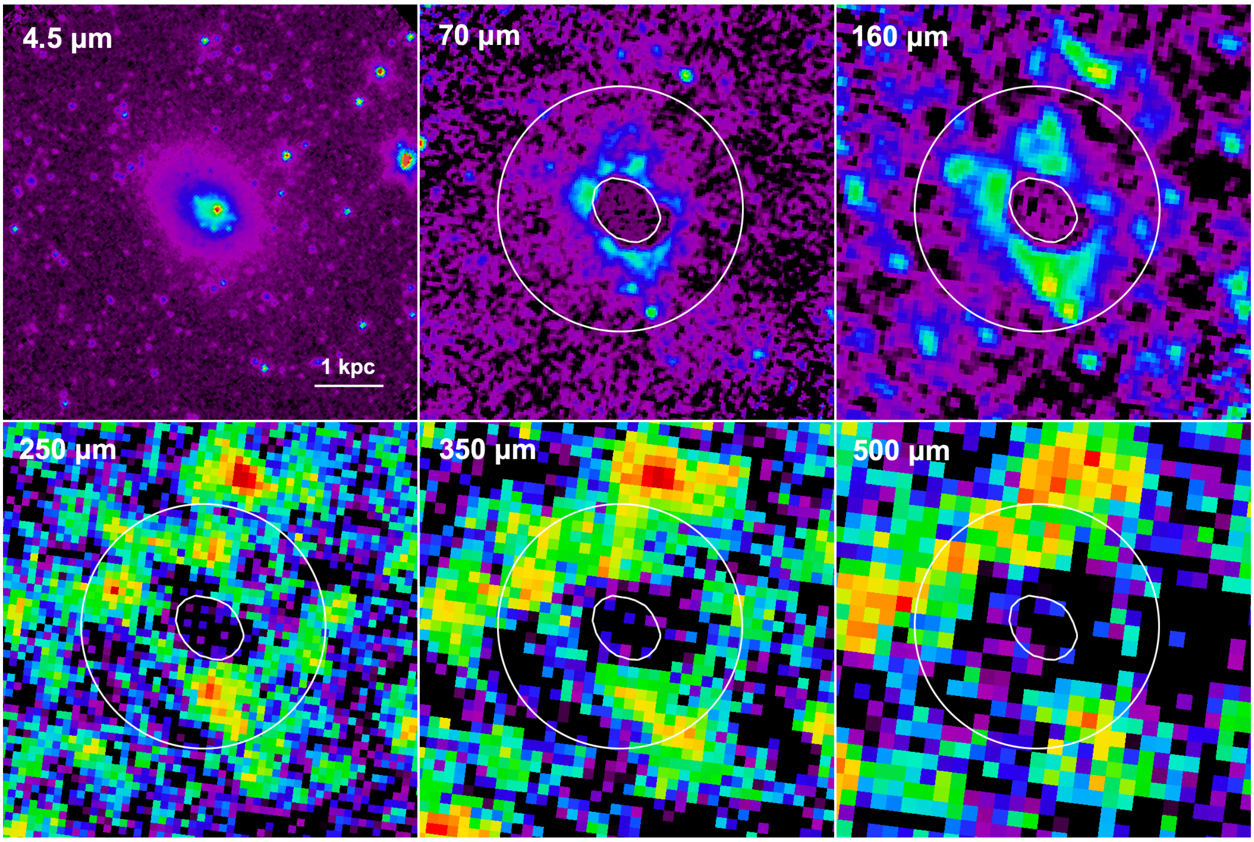

Fig. 2c.— NGC 1705 - display is the same as in Figure 4a

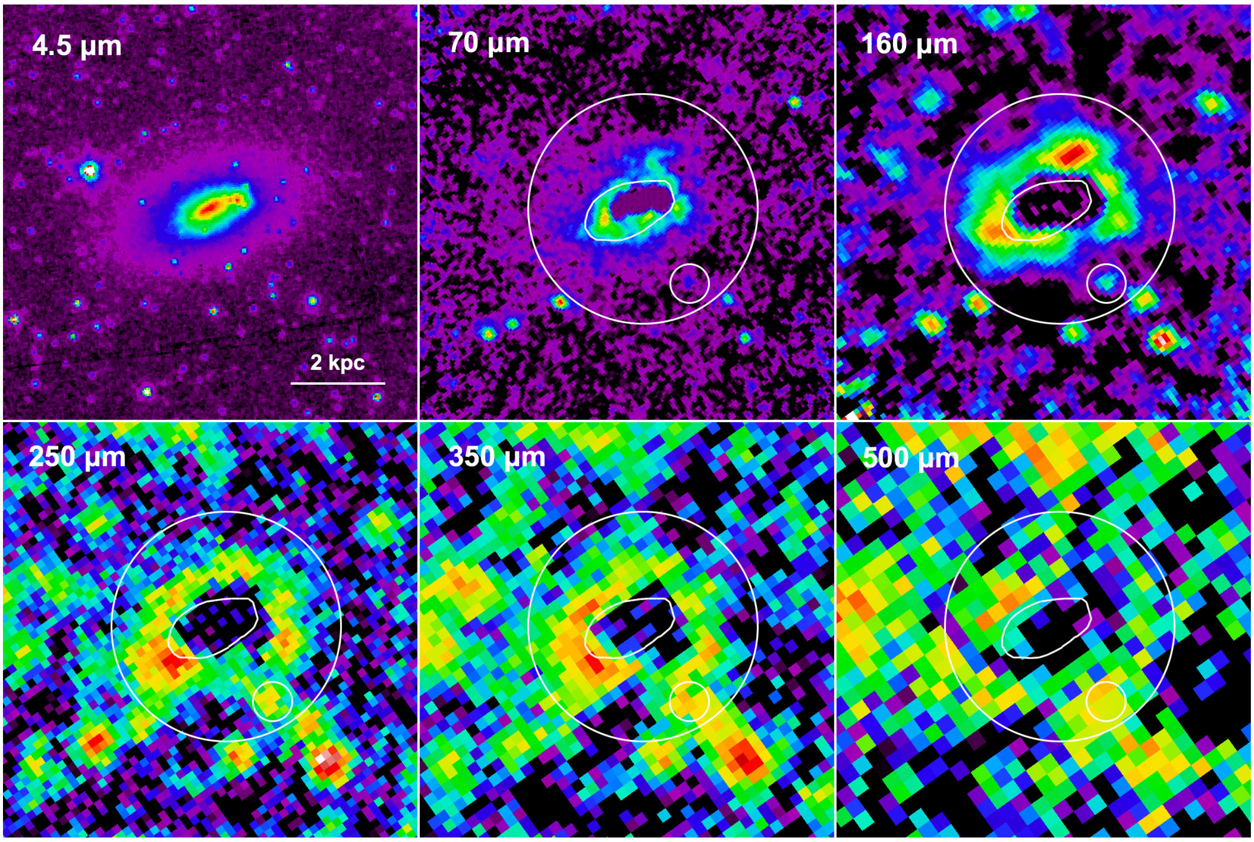

Fig. 2d.— NGC 1800 - display is the same as in Figure 4a, plus one region is masked (smaller white circle).

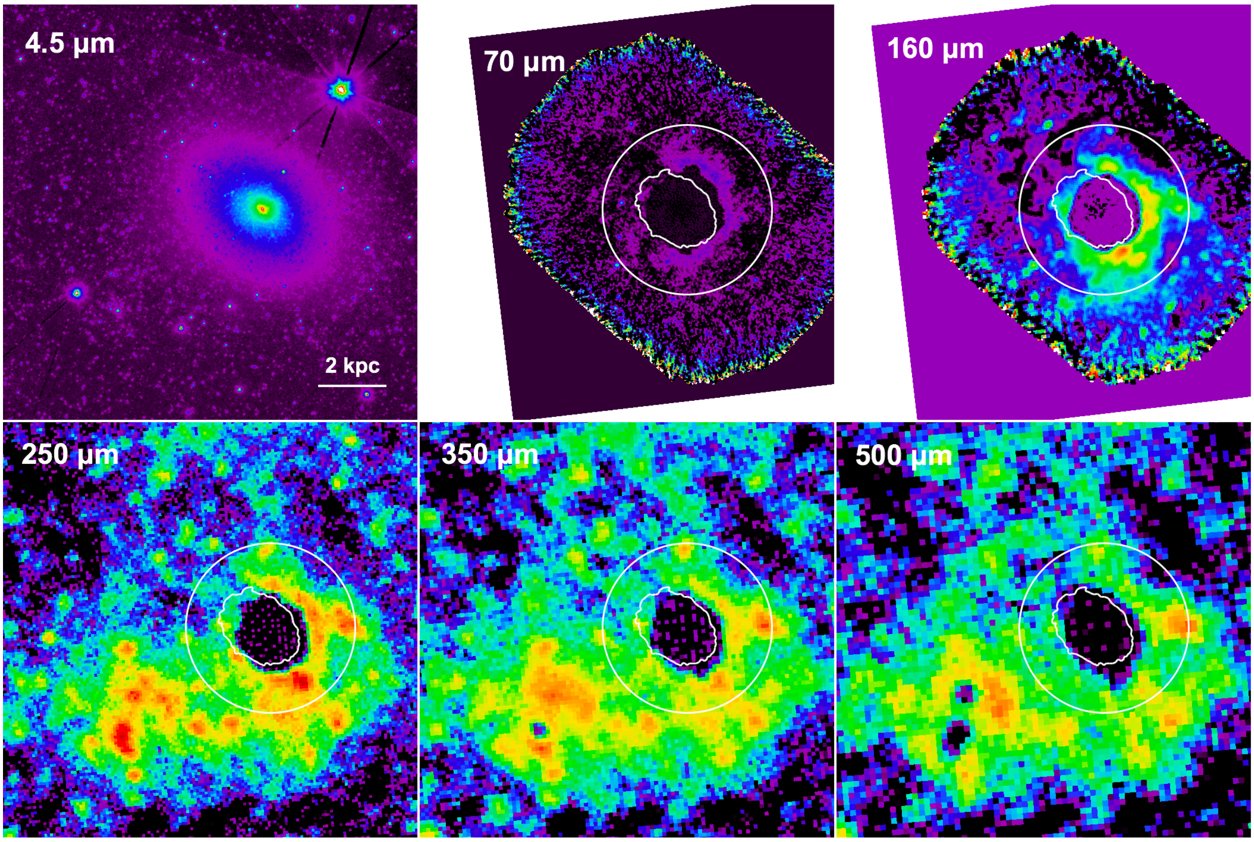

Fig. 2e.— NGC 3077 - display is the same as in Figure 4a

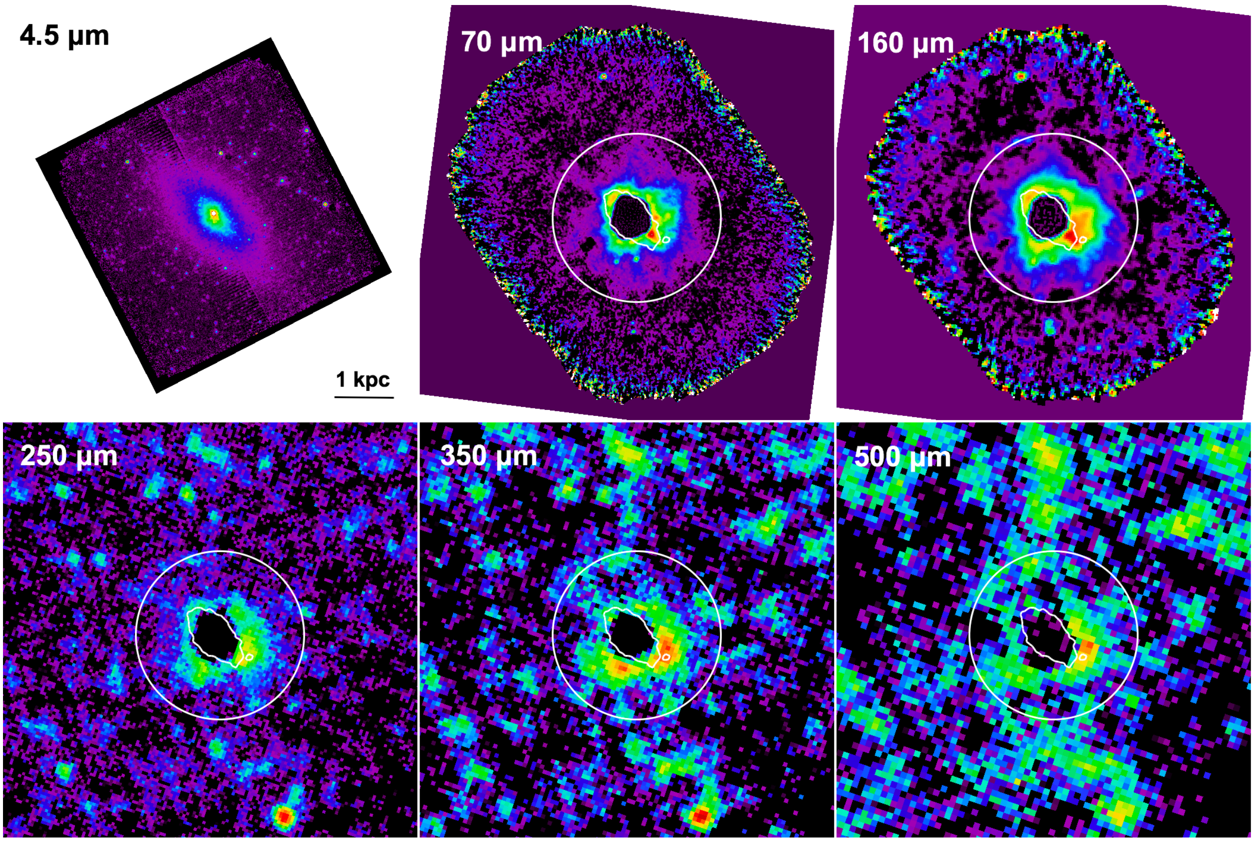

Fig. 2f.— NGC 5253 - display is the same as in Figure 4a

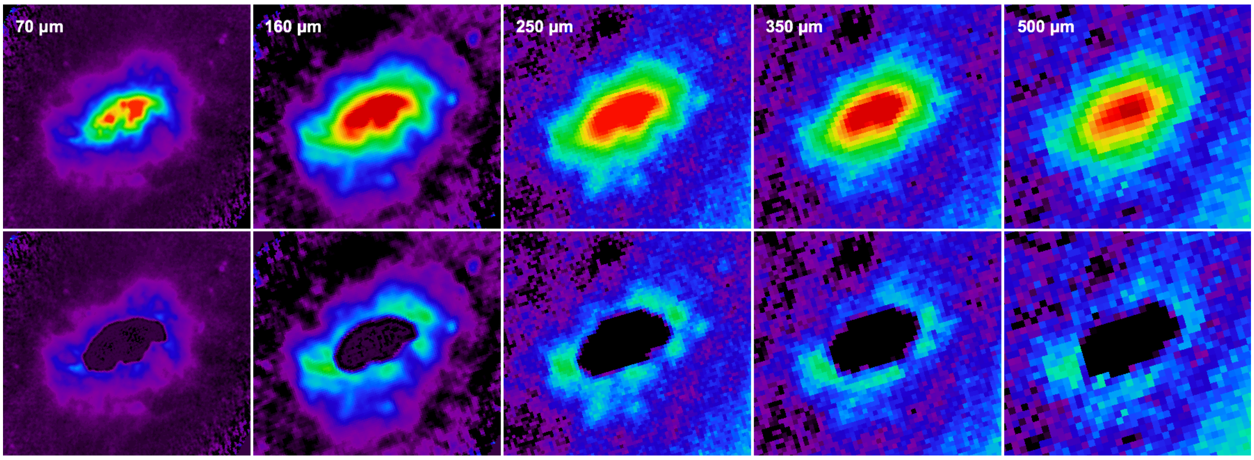

Fig. 3.— PACS and SPIRE maps of NGC 1569 (top row) plus the resulting residual maps (bottom row) after application of our modified CLEAN algorithm. We defined the regions where we applied the CLEAN algorithm in each band based on the disk region for NGC 1569. Since each map has a different pixel scale and slightly different morphology to the bright disk areas, the regions where we applied the CLEAN algorithm are similar in extent but necessarily slightly different from band to band. All maps are shown with logarithmic scale. North is up and east is to the left in all maps.

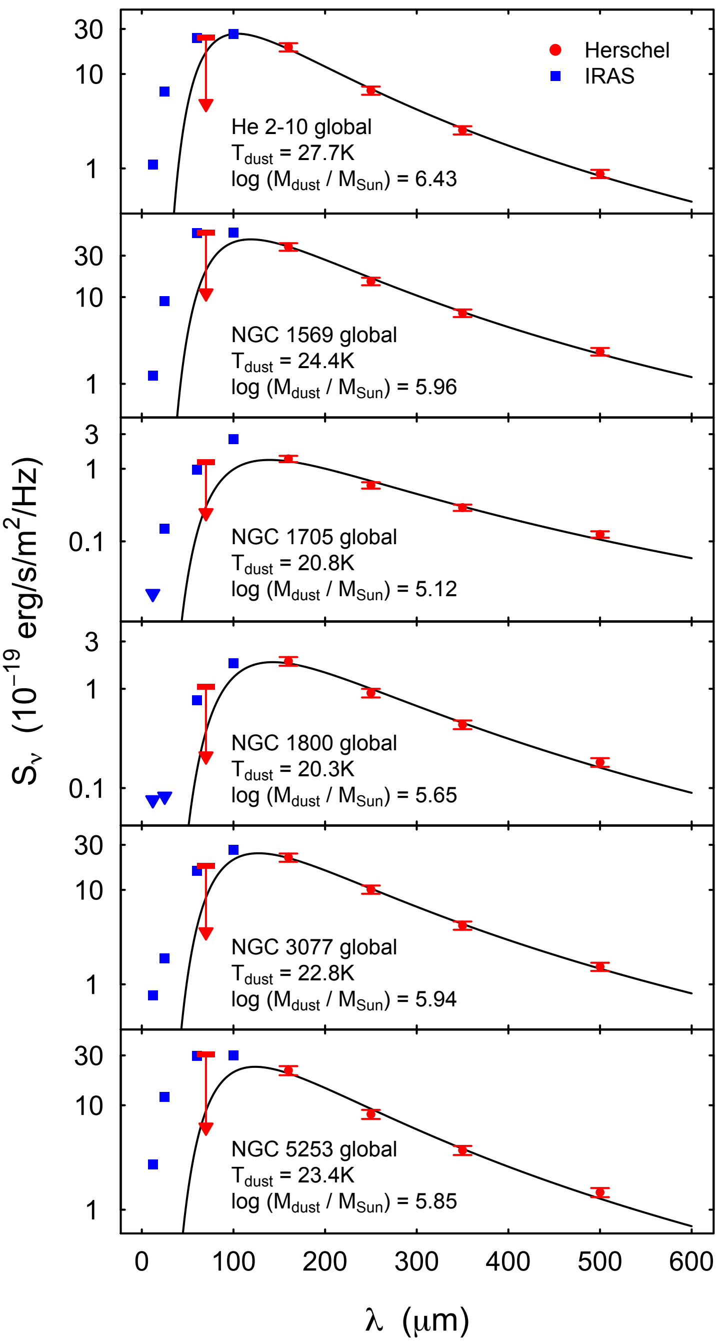

Fig. 4.— Modified blackbody fits for the global galaxy fluxes based on the 70, 160, 250, 350, and 500 μm *Herschel* bands (black lines and red points). In fitting, the 70 μm flux values were treated as upper limits as indicated by the downward arrows. The fit parameters are M_{dust} and T_{dust}. Refer to § 4.4 for details. Blue square points mark the *IRAS* fluxes at 12, 25, 60, and 100 μm (Moshir et al. 1990; Sanders et al. 2003), while blue downward triangles represent upper limits. The modified blackbody fits do not include the *IRAS* flux values since these data are shallower than our *Herschel* maps.

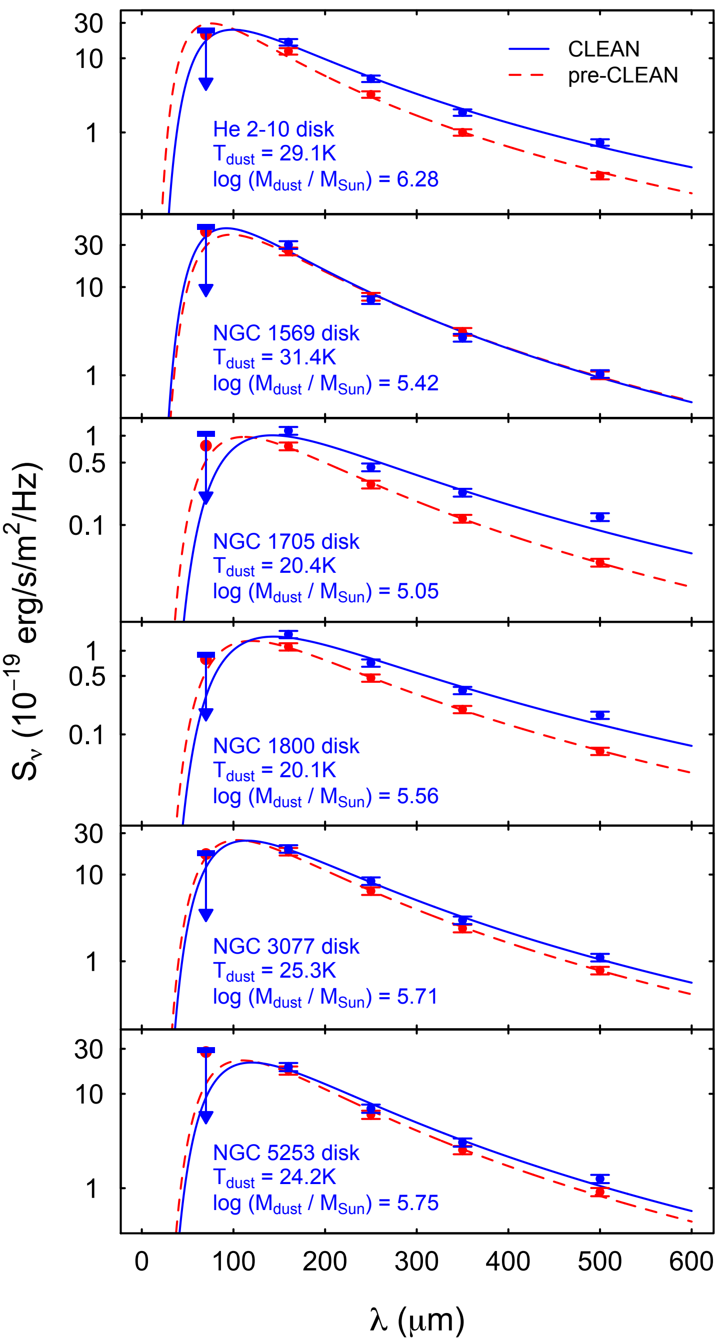

Fig. 5.— Modified blackbody fits for the galaxy disk fluxes based on the 70, 160, 250, 350, and 500 μm *Herschel* bands before (dashed red line) and after (solid blue line) applying our modified CLEAN algorithm. In fitting, the 70 μm flux values were treated as upper limits as indicated by the downward arrows. The fit parameters are M_{dust} and T_{dust}. Refer to § 4.4 for details.

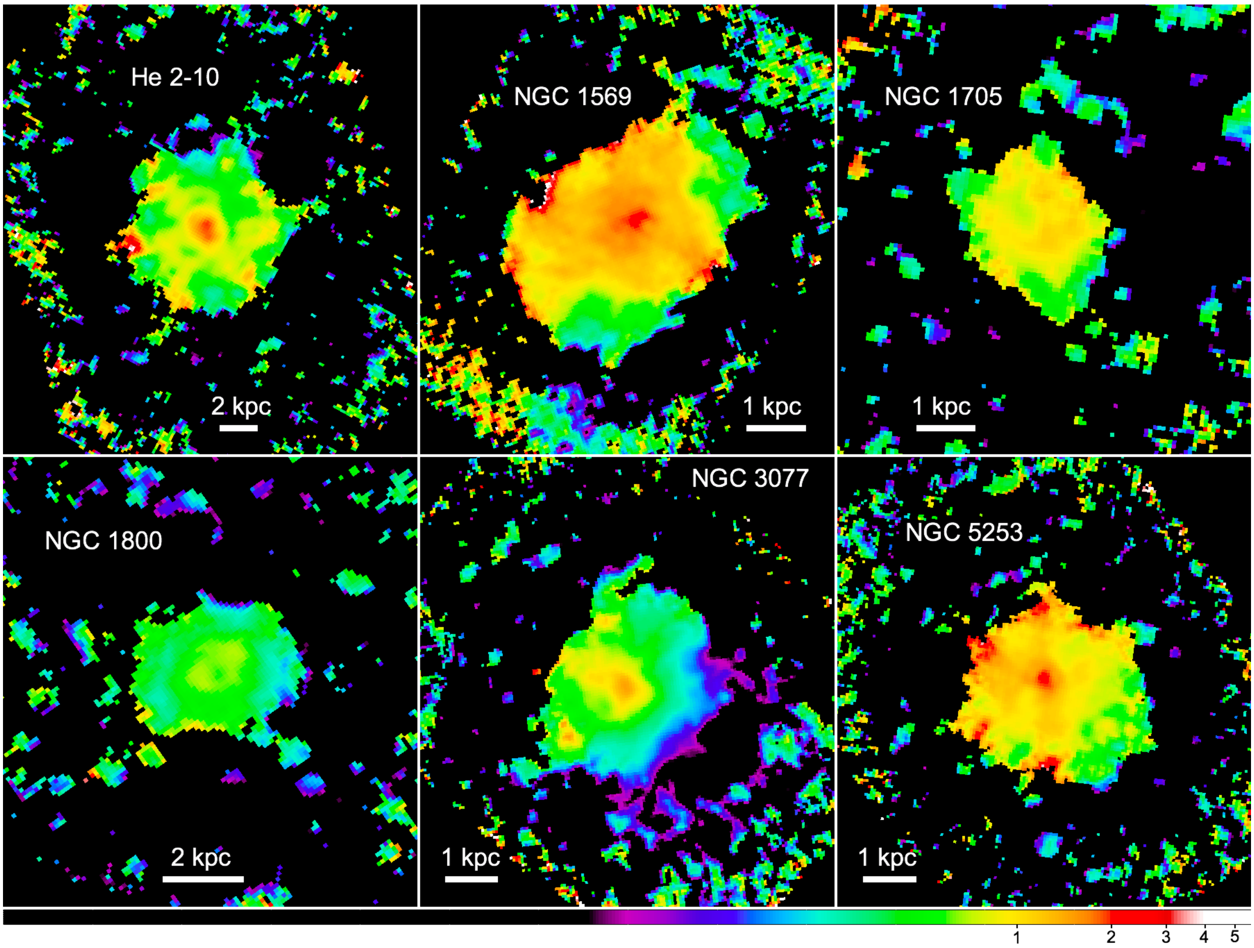

Fig. 6.— 70μm / 160μm ratio maps. All maps are shown with the same logarithmic scale indicated by the color bar. The white bar in each panel indicates the scale of each image. North is up and east is to the left in all images.

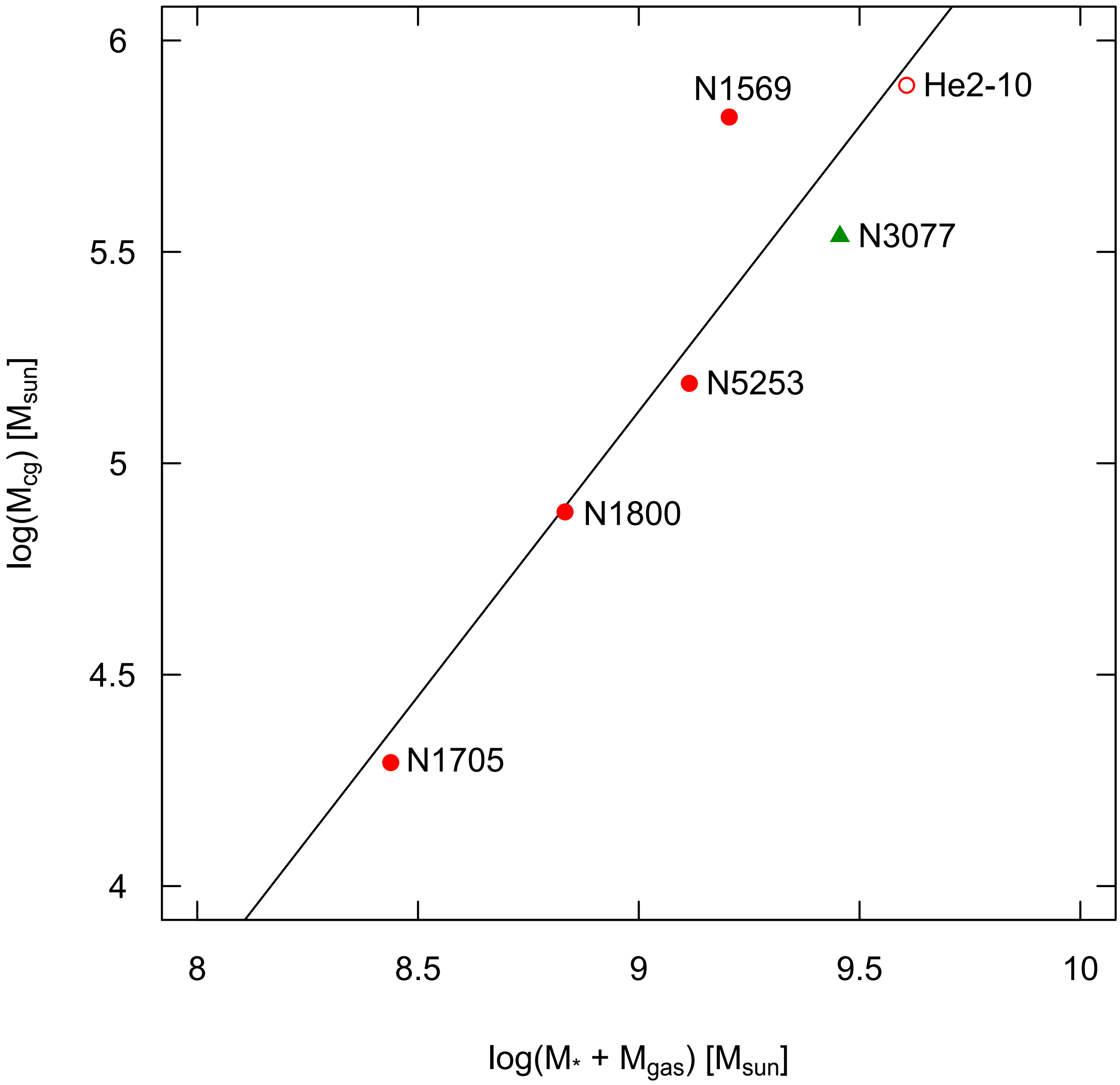

Fig. 7.— Circumgalactic dust mass versus total (stellar plus gas) mass. NGC 3077 is differentiated with a green triangle to indicate the likely tidal contribution to its circumgalactic dust features, and He 2-10 is differentiated with an open circle to indicate the possible AGN contribution to the FIR flux and therefore dust mass. The power law fit $M_{cg} = (M_* + M_{gas})^\alpha$ shown by the solid line has an exponential dependence with $\alpha = 1.3 \pm 0.1$.

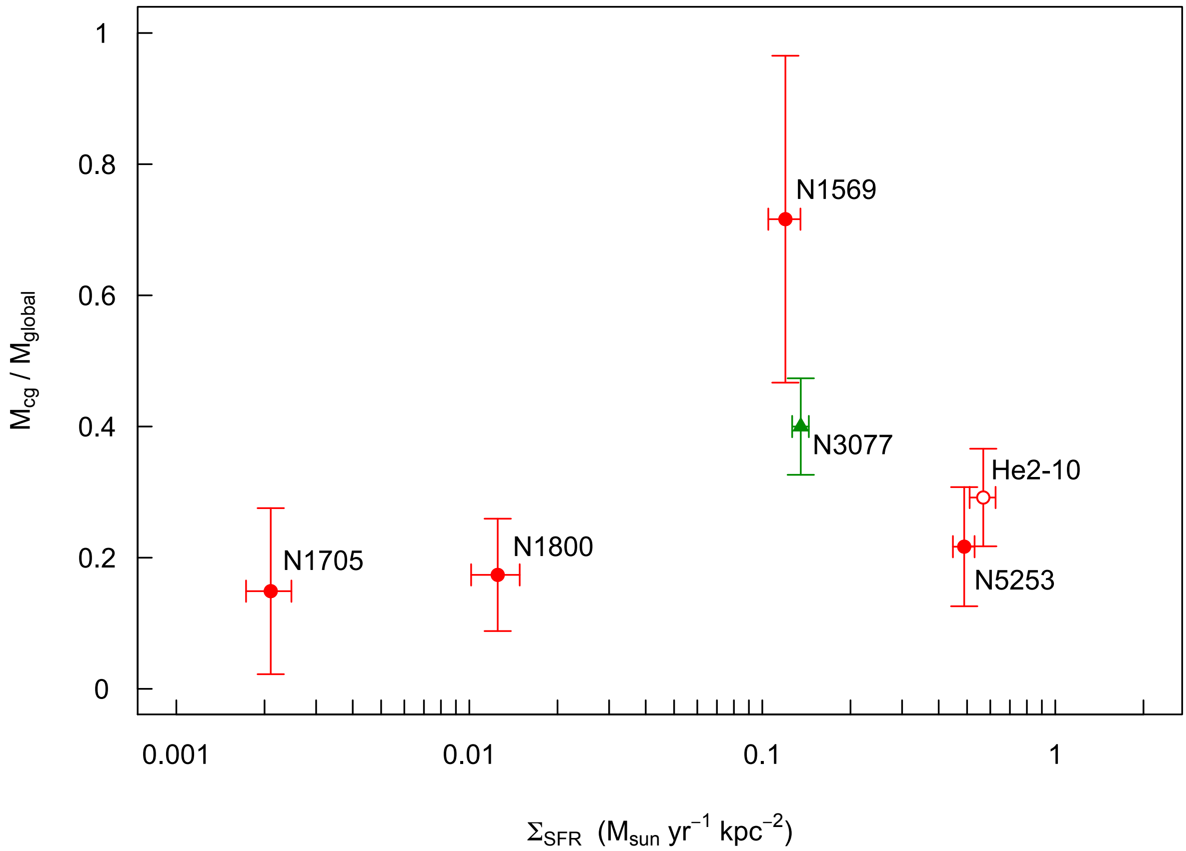

Fig. 8.— Circumgalactic dust mass fraction versus star formation rate surface density based on total IR luminosity (Sanders & Mirabel 1996; Kennicutt 1998), and $R_{H\alpha}$ (Calzetti et al. 2010). The uncertainty in M_{cg}/M_{global} comes from the uncertainties in the SED fitting (§ 4.4), and the uncertainty in Σ_{SFR} comes from the uncertainties in the IRAS fluxes. Meaning of the symbols is the same as in Figure 8.

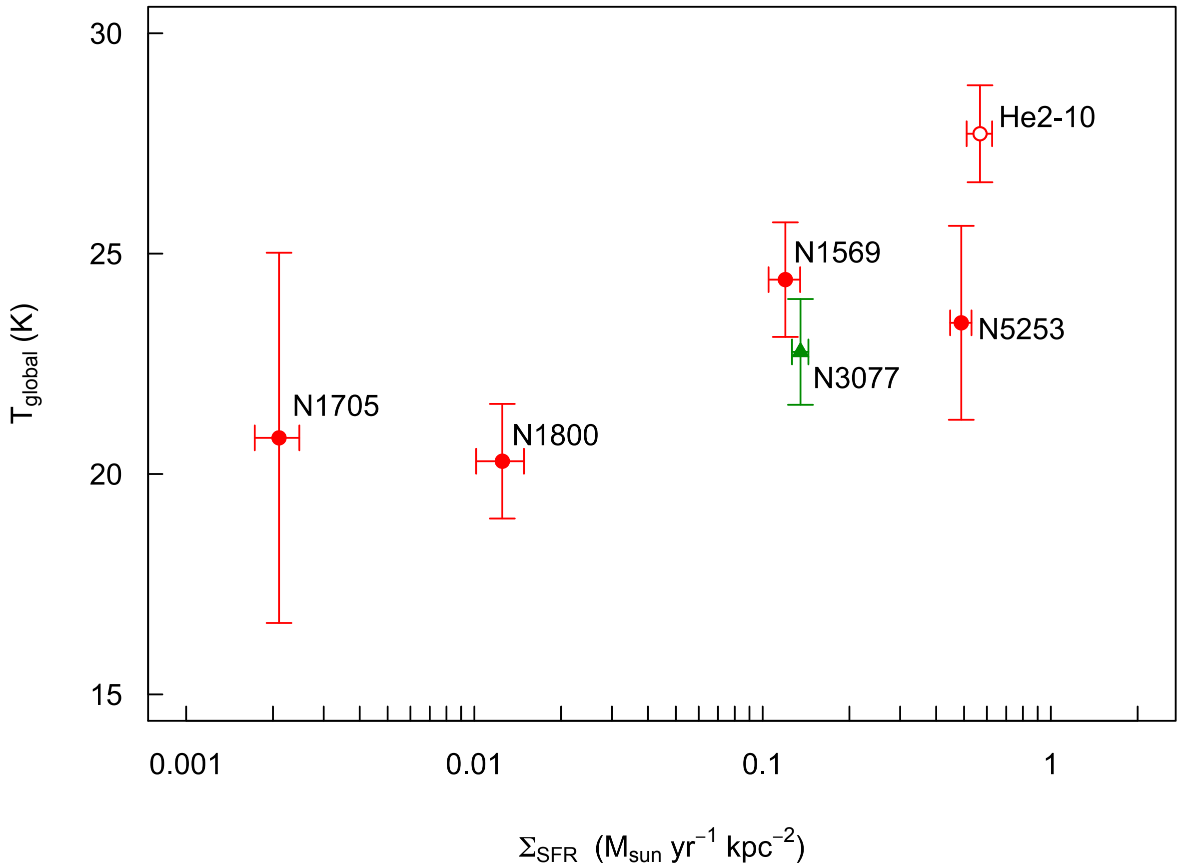

Fig. 9.— Global dust temperature from the modified blackbody fits versus star formation rate surface density based on total IR luminosity (Sanders & Mirabel 1996; Kennicutt 1998), and $R_{H\alpha}$ (Calzetti et al. 2010). The uncertainty in T_{global} comes from the uncertainties in the SED fitting (§ 4.4), and the uncertainty in Σ_{SFR} comes from the uncertainties in the IRAS fluxes. Meaning of the symbols is the same as in Figure 8.

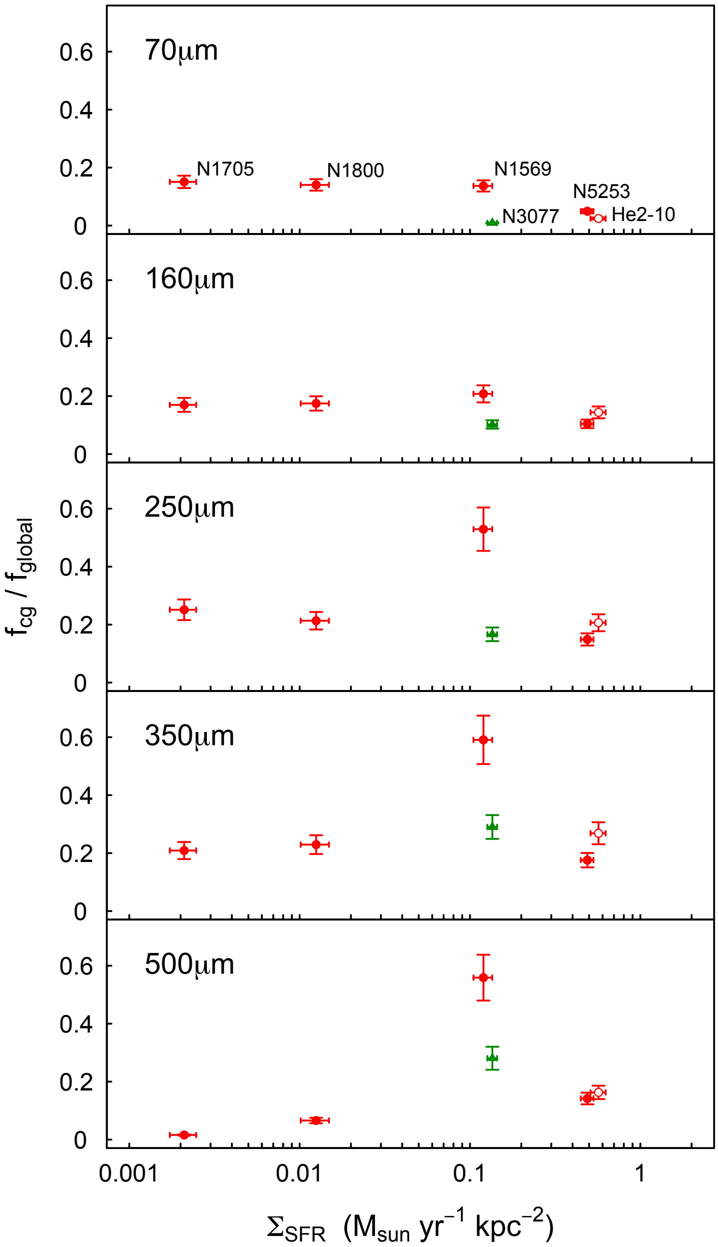

Fig. 10.— Circumgalactic flux fraction in each of the *Herschel* bands versus star formation rate surface density based on total IR luminosity (Sanders & Mirabel 1996; Kennicutt 1998), and $R_{H\alpha}$ (Calzetti et al. 2010). Meaning of the symbols is the same as in Figure 8.

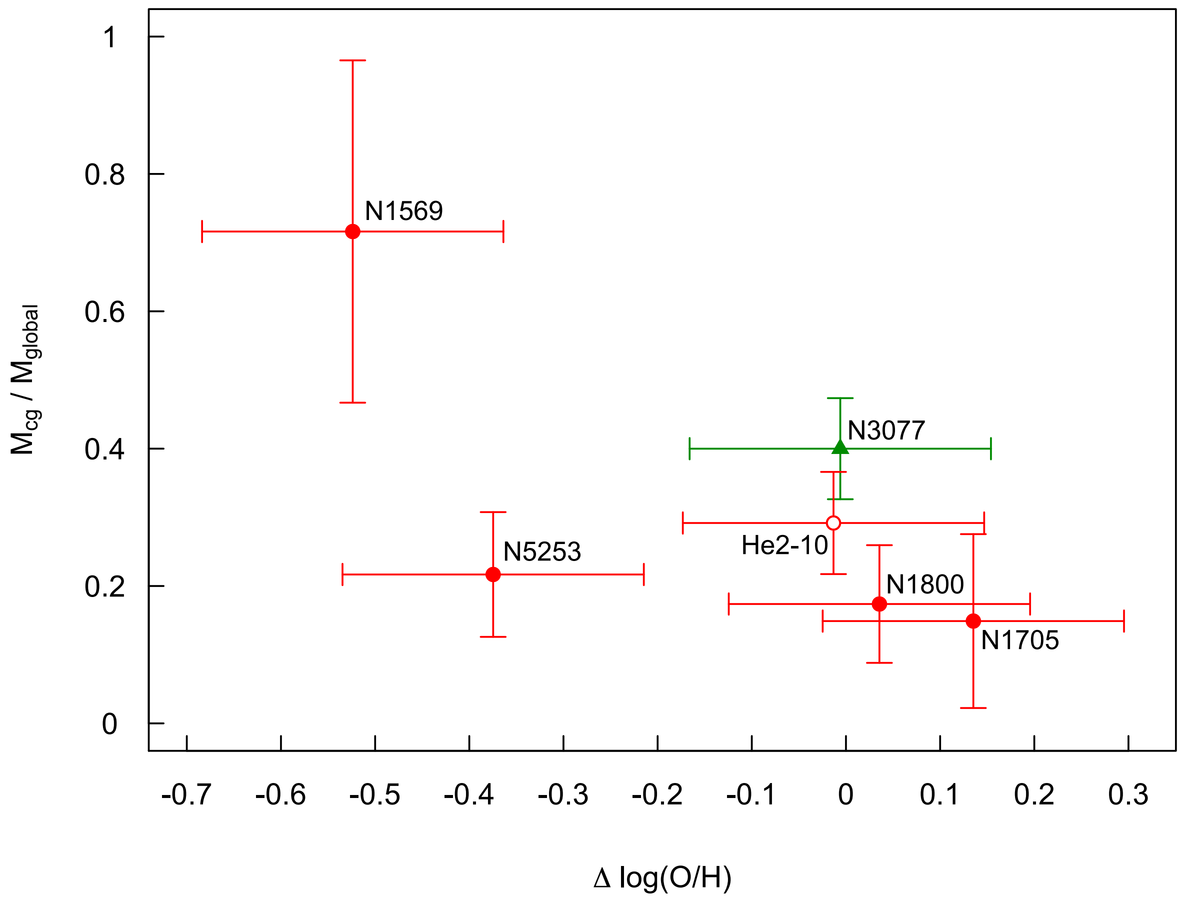

Fig. 11.— Circumgalactic dust mass fraction versus metallicity deficit, Δlog(O/H). Where Δlog(O/H) is the difference between the galaxy metallicity (see Table 1) and the metallicity predicted by the relation derived in Tremonti et al. (2004) between M_* and 12 + log (O/H). The uncertainty in Δlog(O/H) comes from uncertainty in the galaxy metallicity (∼0.1 dex) and uncertainty in converting values to conform with Tremonti et al. (2004) (∼0.06 dex). Meaning of the symbols is the same as in Figure 8.

Table 1. Nearby Dwarf Galaxies and Their Properties

Galaxy	Type [1]	Morph. [2]	D_{25} (') [3]	d (Mpc) [4]	scale (pc/arcsec) [5]	L_{IR} ($10^9 L_\odot$) [6]	12 + log(O/H) [7]	$\log(M_*/M_\odot)$ [8]	Wind/eDIG Ref. [9]
He 2-10	H II + AGN	I0? pec	1.74	10.5	50.9	8.44	8.80	9.5†	1,2,3
NGC 1569	H II	IBm	3.63	3.4	16.3	1.63	8.16	9.14	4,5,6,7,8
NGC 1705	H II	SA0$^-$ pec	1.91	5.1	24.7	0.09*	8.48	8.37†	9,10,11,12
NGC 1800	H II	IB(s)m	2.00	7.4	35.9	0.16*	8.58	8.8	13,14,15
NGC 3077	H II	I0 pec	5.37	3.8	18.6	0.71	8.78	9.44	16,17,18,19
NGC 5253	H II	pec	5.01	3.8	18.3	1.64	8.28	9.05†	13,20,21,22,23

[1]Optical/UV types are galaxies identified by star-forming H II regions (H II) and galaxies containing both an active galactic nucleus (AGN) and star-forming H II regions (H II + AGN).

[2]de Vaucouleurs morphological type from de Vaucouleurs et al. (1991) (hereafter RC3).

[3]Diameter (major axis) in arcminutes based on 25th magnitude B-band observations (RC3).

[4]z-independent distance. References: He 2-10: Tully 1988; NGC 1569: Grocholski et al. 2008; NGC 1705: Tosi et al. 2001; NGC 1800: Tully 1988; NGC 3077: Dalcanton et al. 2009; NGC 5253: Sakai et al. 2004.

[5]Spatial scale assuming the z-independent distance listed here.

[6]IR luminosity (8 - 1000 μm) expressed in units of $10^9 L_\odot$, calculated using equations in Table 1 of Sanders & Mirabel (1996), IRAS flux densities listed in the NASA/IPAC Extragalactic Database (Moshir et al. 1990; Sanders et al. 2003), and the distances listed in this table. The * indicates the calculation of these L_{IR} values included some upper limit IRAS fluxes.

[7]Metallicity derived using the method in Pettini & Pagel (2004) (O3N2), which has then been converted via the prescriptions in Kewley & Ellison (2008) to conform with the metallicities in Tremonti et al. (2004). Uncertainties in the metallicity come from a combination of the method used (~0.1 dex) and the conversion (~0.06 dex). Emission line strength references: He 2-10, NGC 1569, NGC 5253: Kobulnicky et al. 1999; NGC 1705: Moustakas et al. 2010; NGC 1800: Moustakas & Kennicutt 2006; NGC 3077: McQuade et al. 1995.

[8]Stellar masses calculated using the M/L derived from Bell et al. (2003), Two Micron All Sky Survey K magnitudes (Skrutskie et al. 2003), and optical colors (either B-V or B-R). The † indicates masses adopted from Zastrow et al. (2013) calculated using this method. We used the optical colors found in RC3 to calculate the masses of NGC 1569, NGC 1800, and NGC 3077.

[9]Selected references to a galactic wind or extraplanar diffuse ionized gas (eDIG): (1) Méndez et al. 1999; (2) Johnson et al. 2000; (3) Kobulnicky & Martin 2010; (4) Waller 1991; (5) Hunter et al. 1993; (6) Heckman et al. 1995; (7) della Ceca et al. 1996; (8) Westmoquette et al. 2008; (9) Meurer et al. 1989; (10) Meurer et al. 1992; (11) Meurer et al. 1998; (12) Heckman et al. 2001; (13) Marlowe et al. 1995; (14) Hunter 1996; (15) Rasmussen et al. 2004; (16) Thronson et al. 1991; (17) Martin 1998; (18) Ott et al. 2003; (19) Calzetti et al. 2004; (20) Calzetti et al. 1999; (21) Strickland & Stevens 1999; (22) Kobulnicky & Skillman 2008; (23) Zastrow et al. 2011

Table 2. *Herschel Space Observatory* Data

Galaxy	Instrument (PACS/SPIRE)	t^a_{int} (hrs)	Obs. ID(s)^b	Principal Investigator (OT/KPGT/SDP/KPOT)$^{(c)}$
He 2-10	PACS	6.56	1342244883-89	Veilleux, S. (OT2)
	SPIRE	0.07	1342196888	Madden, S. (KPGT)
NGC 1569	PACS	6.56	1342243817-22	Veilleux, S. (OT2)
	SPIRE	0.15	1342193013	Madden, S. (KPGT)
NGC 1705	PACS	6.56	1342236656-62	Veilleux, S. (OT1)
	SPIRE	0.20	1342186114	Madden, S. (SDP)
NGC 1800	PACS	6.56	1342263895-901	Veilleux, S. (OT2)
	SPIRE	0.16	1342240035	Veilleux, S. (OT2)
NGC 3077	PACS	8.74	1342243845-51	Veilleux, S. (OT2)
	SPIRE	0.58	1342193015	Kennicutt, R. C., Jr. (KPOT)
NGC 5253	PACS	8.74	1342249927-33	Veilleux, S. (OT2)
	SPIRE	0.29	1342203078	Madden, S. (KPGT)

[a]Total observation integration time in hours.

[b]*Herschel* Observation ID number(s).

[c]*Herschel* Open Time (OT), Key Programme Guaranteed Time (KPGT), Science Demonstration Phase (SDP), or Key Programme Open Time (KPOT).

Table 3. Ancillary Data

Galaxy	Band	t_{int}^{a} (s)	Observatory/Instrument	Obs. ID(s)[b]	PI(s)[c]
He 2-10	Hα	1200	Magellan/MMTF	···	Oey, S.
	4.5 μm	41.6	*Spitzer*/IRAC	4329472	Rieke, G.
	8.0 μm	41.6	*Spitzer*/IRAC	4329472	Rieke, G.
	24 μm	2.62	*Spitzer*/MIPS	4347904	Rieke, G.
NGC 1569	Hα	300	KPNO/Bok	···	Martin, C. L.
	4.5 μm	52	*Spitzer*/IRAC	4434944	Fazio, G.
	8.0 μm	52	*Spitzer*/IRAC	4434944	Fazio, G.
	24 μm	2.62	*Spitzer*/MIPS	4435456	Fazio, G.
NGC 1705	Hα	1200	Magellan/MMTF	···	Oey, S.
	4.5 μm	214.4	*Spitzer*/IRAC	5535744, 5536000	Kennicutt, R. C., Jr.
	8.0 μm	214.4	*Spitzer*/IRAC	5535744, 5536000	Kennicutt, R. C., Jr.
	24 μm	3.67	*Spitzer*/MIPS	5549312	Kennicutt, R. C., Jr.
NGC 1800	Hα	901.2	KPNO/Bok	···	Martin, C. L.
	4.5 μm	428.8	*Spitzer*/IRAC	22530304, 22530560, 22530816, 22531072	Kennicutt, R. C., Jr.
	8.0 μm	428.8	*Spitzer*/IRAC	22530304, 22530560, 22530816, 22531072	Kennicutt, R. C., Jr.
	24 μm	3.67	*Spitzer*/MIPS	22624000	Kennicutt, R. C., Jr.
NGC 3077	Hα	1000	KPNO/Bok	···	Kennicutt, R. C., Jr.
	4.5 μm	4758.4 (804)[d]	*Spitzer*/IRAC	4331520, 22000640, 22354944, 22357760, 22358016, 22539520, 22539776	Kennicutt, R. C., Jr., Neff, S., Rieke, G.
	8.0 μm	4758.4 (804)[d]	*Spitzer*/IRAC	4331520, 22000640, 22354944, 22357760, 22358016, 22539520, 22539776	Kennicutt, R. C., Jr., Neff, S., Rieke, G.
	24 μm	3.67	*Spitzer*/MIPS	17597696	Rieke, G.
NGC 5253	Hα	1200	Magellan/MMTF	···	Oey, S., Veilleux, S., Zastrow, J.
	4.5 μm	249.6	*Spitzer*/IRAC	4386048	Houck, J. R.
	8.0 μm	249.6	*Spitzer*/IRAC	4386048	Houck, J. R.
	24 μm	3.67	*Spitzer*/MIPS	22679040	Kennicutt, R. C., Jr.

[a]Total integration time in seconds.

[b]Observation ID number(s).

[c]Principal Investigator(s).

[d]Total IRAC mosaic integration time for NGC 3077 (typical mosaic pixel integration time).

Table 4. Global, Disk, and Circumgalactic Fluxes[a]

Galaxy	Global[b] (Jy)					Disk[c] (Jy)					Circumgalactic[d] (Jy)				
	70	160	250	350	500	70	160	250	350	500	70	160	250	350	500
He 2-10	24.206	19.260	6.696	2.543	0.878	23.616	16.488	5.313	1.860	0.735	0.590	2.772	1.383	0.683	0.143
NGC 1569	55.466	37.953	15.189	6.539	2.355	47.879	30.068	7.149	2.676	1.039	7.587	7.885	8.040	3.863	1.316
NGC 1705	1.234	1.372	0.593	0.292	0.125	1.048	1.139	0.444	0.231	0.123	0.186	0.233	0.149	0.061	0.002
NGC 1800	1.048	1.900	0.909	0.436	0.182	0.901	1.568	0.715	0.336	0.170	0.147	0.332	0.194	0.100	0.012
NGC 3077	17.897	22.071	10.115	4.204	1.539	17.732	19.815	8.430	2.984	1.107	0.165	2.256	1.685	1.220	0.432
NGC 5253	30.740	21.540	8.212	3.709	1.466	29.221	19.294	6.989	3.057	1.258	1.519	2.246	1.223	0.652	0.208

[a]Tabulated fluxes have a calibration uncertainty of 10%.

[b]Global fluxes measured in the 250, 350, and 500 μm SPIRE maps include background corrections.

[c]Disk fluxes are calculated: Global - Circumgalactic. (see § 4.3).

[d]Circumgalactic fluxes are measured in the CLEAN residual images. (see § 4.3).

Table 5. Spectral Energy Distribution Fits

	Global			Disk			Circumgalactic[a]
Galaxy	$\log(M_{global}\ /\ M_{\odot})$	β^{b}	T_{dust}	$\log(M_{disk}\ /\ M_{\odot})$	β^{b}	T_{dust}	$\log(M_{cg}\ /\ M_{\odot})$
He 2-10	$6.43^{+0.038}_{-0.042}$	2.00	27.7 ± 1.1	$6.28^{+0.093}_{-0.118}$	2.00	29.1 ± 2.4	$5.89^{+0.099}_{-0.128}$
NGC 1569	$5.96^{+0.057}_{-0.066}$	2.00	24.4 ± 1.3	$5.42^{+0.120}_{-0.166}$	2.00	31.4 ± 4.5	$5.82^{+0.130}_{-0.186}$
NGC 1705	$5.12^{+0.149}_{-0.228}$	2.00	20.8 ± 4.2	$5.05^{+0.242}_{-0.594}$	2.00	20.4 ± 5.3	$4.29^{+0.267}_{-0.825}$
NGC 1800	$5.65^{+0.074}_{-0.090}$	2.00	20.3 ± 1.3	$5.56^{+0.163}_{-0.265}$	2.00	20.1 ± 5.0	$4.89^{+0.174}_{-0.295}$
NGC 3077	$5.94^{+0.045}_{-0.050}$	2.00	22.8 ± 1.2	$5.71^{+0.060}_{-0.070}$	2.00	25.3 ± 1.0	$5.54^{+0.073}_{-0.088}$
NGC 5253	$5.85^{+0.104}_{-0.136}$	2.00	23.4 ± 2.2	$5.75^{+0.121}_{-0.168}$	2.00	24.2 ± 2.4	$5.19^{+0.152}_{-0.236}$

[a]Circumgalactic dust mass was determined by subtracting the disk value from the global value (see § 4.4).

[b]β values were fixed at 2.00 (see § 4.4).